



## Modelling 18650-type lithium-ion battery fires using surrogate fuels

Hosein Sadeghi <sup>a</sup>, Francesco Restuccia <sup>a,b</sup>,\*

<sup>a</sup> Department of Engineering, King's College London, Strand, London WC2R 2LS, UK

<sup>b</sup> The Faraday Institution, Quad One, Harwell Science and Innovation Campus, Didcot, UK

### ARTICLE INFO

**Keywords:**

Combustion modelling  
Lithium-ion battery  
Thermal runaway  
Reacting vent gas  
Surrogate fuel

### ABSTRACT

This study proposes a simplified combustion modelling approach for 18650-type lithium-ion battery fires in thermal runaway by using surrogate fuels instead of the complex fuel mixture of the vent gases. Twelve different fuels were compared through 1-D premixed and counterflow diffusion flame simulations to identify the most suitable surrogate fuel for batteries with LCO, LFP, and NMC cathodes. The investigation focused on batteries at 100% state of charge (SOC), which pose a higher risk of thermal runaway and greater subsequent hazards compared to lower SOCs. For 1-D flames, CH<sub>4</sub>/CO<sub>2</sub>/CO showed the best performance for all the battery chemistries studied. The battery flame was further validated with 3-D simulations and it was shown that the use of surrogate fuel significantly reduced CPU time by at least 55% compared to the two-step kinetic modelling of the vent gas, which is the common approach used in the literature. This efficiency was achieved while maintaining acceptable levels of accuracy, with maximum errors of 12.2% and 9.5% in flame scalar fields and radiative heat flux, respectively. These findings demonstrate that this approach holds promise for improving computational efficiency in CFD simulations of lithium-ion battery fires in thermal runaway, potentially enhancing the prediction of such events.

### 1. Introduction

Lithium-ion batteries (LIBs) have witnessed a surging demand as a power source for consumer electronics, electric vehicles, and stationary energy storage systems. Renowned for their superior energy density and extended lifespan compared to conventional nickel-cadmium batteries, lithium-ion batteries have emerged as the preferred choice for high-energy density applications. However, the widespread adoption of lithium-ion batteries has also introduced new safety concerns and challenges. The paramount safety concern is the potential occurrence of thermal runaway. This phenomenon arises when the battery's heat generation during charging, discharging, or storage surpasses the ability to dissipate it swiftly, resulting in overheating and ultimately culminating in a catastrophic failure of the battery. This occurrence can be triggered by mechanical [1], thermal [2], or electrical abuse [3] and be sustained by internal exothermic reactions. As the temperature of the battery increases, there is a potential for the decomposition of the components [4], resulting in vent gases that are mixtures of combustible gases [5,6]. These gases, characterised by their elevated temperatures, can ultimately contribute to the ignition of severe fires. It is important to note that this risk is not limited to specific cases, as it encompasses a wide range of devices such as smartphones, laptops, electric vehicles, and battery energy storage systems, regardless of operating conditions.

Furthermore, with the increasing proliferation of these systems [7], this risk becomes an even more pressing concern.

The fire risk associated with lithium-ion batteries has prompted dedicated research efforts aimed at investigating thermal runaway and battery fires. These studies encompass various aspects, including the detection and measurement of vent gases during thermal runaway [5], the influence of environmental conditions on thermal runaway [8,9], and the effects of battery state of charge [10] on thermal runaway characteristics. Experimental measurements, such as those by Lopez et al. [11] and Zhong et al. [12], have laid the foundation for numerical modelling of thermal runaway, enabling the validation of results. The modelling of thermal runaway can be classified into three main groups: (1) Electrochemical modelling [13,14], which focuses on internal electrochemical reactions and heat generation within the battery; (2) Combustion modelling [15–17], which investigates the flame and its properties; and (3) Coupled modelling [15], which integrates both electrochemical and combustion modelling aspects.

In realistic combustion scenarios, the oxidation process of fuels involves numerous chain reactions, ranging from tens to thousands. The development of these reaction pathways necessitates specialised knowledge and expertise in chemical kinetic modelling. In the literature, some pioneering researchers have extensively analysed the

\* Corresponding author at: Department of Engineering, King's College London, Strand, London WC2R 2LS, UK.  
E-mail address: [francesco.restuccia@kcl.ac.uk](mailto:francesco.restuccia@kcl.ac.uk) (F. Restuccia).

<b>Nomenclature</b>		<b>Abbreviations</b>	
<i>A</i>	Pre-exponential constant in Arrhenius expression [ $\text{cm}^3 \text{ mol}^{-1} \text{ s}^{-1}$ ]	CPU	Index for CPU time
<i>B</i>	Number of measuring points in 3-D simulations [-]	c	Cell-by-cell
<i>C</i>	Total number of cells in 3-D simulations [-]	d	Number of carbon atoms in hydrocarbon fuels
<i>c<sub>p</sub></i>	Specific heat capacity at constant pressure per unit mass [ $\text{J kg}^{-1} \text{ K}^{-1}$ ]	e	Number of hydrogen atoms in hydrocarbon fuels
<i>c<sub>n</sub></i>	Molar concentration of reactant <i>n</i> [-]	f	Number of oxygen atoms in hydrocarbon fuels
<i>D<sub>ki</sub></i>	Ordinary diffusion coefficient of species <i>k</i> in multi-component mixture [ $\text{m}^2 \text{ s}^{-1}$ ]	det	Detailed kinetic mechanism
<i>D<sub>ki</sub><sup>T</sup></i>	Thermal diffusion coefficient of species <i>k</i> in multi-component mixture [ $\text{kg m}^{-1} \text{ s}^{-1}$ ]	i	Index for the number of equivalence ratio
<i>E<sub>a</sub></i>	Activation energy in Arrhenius expression [ $\text{kcal mol}^{-1}$ ]	j	Index for number of cells
<i>h<sub>k</sub></i>	Specific enthalpy of species <i>k</i> [ $\text{J kg}^{-1}$ ]	k	Index for chemical species
<i>j<sub>k</sub></i>	Diffusive mass flux of species <i>k</i> [ $\text{kg m}^{-2} \text{ s}^{-1}$ ]	Mix	Fuel mixture
<i>M</i>	Number of reactions [-]	m	Index for number of reactions
<i>N</i>	Number of reactants [-]	n	Index for number of reactants
<i>R</i>	Ideal gas constant [ $\text{J mol}^{-1} \text{ K}^{-1}$ ]	o	Overall
<i>p</i>	Pressure [atm]	r	Radiative heat flux
<i>r</i>	Radius [m]		
<i>S<sub>L</sub></i>	Laminar flame speed [ $\text{m s}^{-1}$ ]		
<i>T</i>	Temperature [K]		
<i>u</i>	Axial velocity [ $\text{m s}^{-1}$ ]		
<i>V</i>	Scaled axial velocity [ $\text{s}^{-1}$ ]		
<i>v</i>	Radial velocity [ $\text{m s}^{-1}$ ]		
<i>W<sub>k</sub></i>	Molecular weight of species <i>k</i> [ $\text{kg mol}^{-1}$ ]		
<i>W</i>	Mean molecular weight of the mixture [ $\text{kg mol}^{-1}$ ]		
<i>X<sub>k</sub></i>	Mole fraction of species <i>k</i> [ $\text{mol mol}_{\text{mix}}^{-1}$ ]	CFD	Computational fluid dynamics
<i>Y<sub>k</sub></i>	Mass fraction of species <i>k</i> [ $\text{kg kg}_{\text{mix}}^{-1}$ ]	IHR	Integral heat release
<i>Z</i>	Number of equivalence ratios [-]	LCO	Lithium cobalt oxide
<i>z</i>	Axial coordinate [m]	LFP	Lithium ferro phosphate
<b>Greek letters</b>		LIB	Lithium-ion battery
$\beta$	Temperature exponent of the global reactions [-]	MAE	Mean absolute error
$\beta_m$	Temperature exponent of reaction <i>m</i> [-]	NMC	Lithium nickel manganese cobalt oxide
$\lambda$	Thermal conductivity [ $\text{W m}^{-1} \text{ K}^{-1}$ ]	SOC	State of charge
$\kappa$	Reaction rate [ $\text{cm}^3 \text{ mol}^{-1} \text{ s}^{-1}$ ]		
$\mu$	Dynamic viscosity [ $\text{kg m}^{-1} \text{ s}^{-1}$ ]		
$\nu_n$	Stoichiometric coefficient of reactant <i>n</i> [-]		
$\rho$	Density [ $\text{kg m}^{-3}$ ]		
$\phi$	Equivalence ratio [-]		
$\chi$	Arbitrary parameter representing mole fractions or temperature for calculating errors [variable]		
$\omega_k$	Reaction rate of species <i>k</i> [ $\text{mol m}^{-3} \text{ s}^{-1}$ ]		
<b>Subscripts</b>			
1S	One-step kinetic mechanism		
2S	Two-step kinetic mechanism		
adb	Adiabatic		
avg	Average		
<i>b</i>	Index for number of measuring points in 3-D simulations		

oxidation of hydrocarbon fuels and subsequently formulated detailed kinetic mechanisms to describe these processes [18]. Furthermore, this scientific approach has been extended to other fuels such as H<sub>2</sub> [19]. Not limited to these cases, the study of combustion kinetic mechanisms is still a rich area of research focus.

Given that the battery vent gas emitted during thermal runaway comprises a mixture of hydrocarbon fuels, H<sub>2</sub>, and CO, it is possible to model the oxidation of this gaseous mixture using existing detailed kinetic mechanisms such as GRI [20–22], SanDiego [23,24], NUIG [25, 26], Sun [6,27], Aramco [26,28], CRECK [26,29], JetSurF [26,30] and Healy [31,32]. These studies collectively contribute to enhancing our understanding of combustion behaviour, flame characteristics, and explosion hazards associated with the battery vent gases.

While detailed kinetic mechanisms are the most accurate approach for combustion modelling, their application in 3-D and large-scale computational fluid dynamics (CFD) simulations becomes impractical due to the large number of reactions involved. For instance, the combustion of Methane alone could consist of 325 reactions and 53 species [20]. To address this limitation, reduced kinetic mechanisms serve as a viable alternative. Cellier et al. [24] recognised this need in the context of LIB fire modelling and presented a reduced kinetic mechanism specifically designed for cells with LCO, LFP, and NMC cathodes. In [24], the vent gas compositions of Golubkov et al. [5,33], Koch et al. [34] and the Federal Aviation Administration (FAA) [35] were considered as the fuel mixture, and the SanDiego kinetic mechanism was employed as a benchmark solution. As reported in [24], although the reduced kinetic mechanism exhibited satisfactory performance, the computational time for 3-D simulations remained impractical for many applications.

To further simplify the combustion modelling, researchers have explored more concise approaches, such as employing few-step kinetic mechanisms with marginal errors. Kim et al. [15] and Kong et al. [16] utilised two-step kinetic mechanisms for H<sub>2</sub> and hydrocarbon fuels,

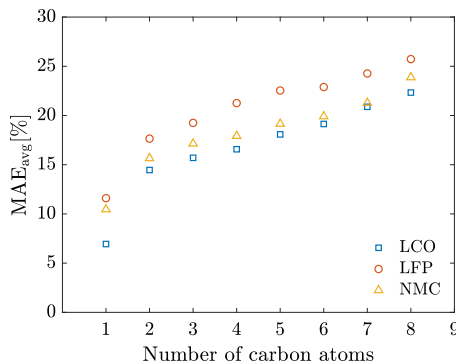


Fig. 1. Average mean absolute errors versus number of carbon atoms in Alkanes examined in the initial evaluations.

while Vendra et al. [36] adopted a one-step kinetic mechanism for all the fuels in the vent gas. Although the one-step kinetic mechanism represents the simplest approach, its application becomes computationally expensive when multiple fuels are present in the vent gas. In a different approach, Voigt et al. [37] proposed an empirical model to predict heat release and gas temperature. Although it was a computationally inexpensive approach for CFD simulations, the results showed considerable deviations from the experimental data and were limited to very specific scenarios.

The current study aims to provide a computationally inexpensive, but accurate combustion modelling approach for the 1860-type LIB fires in thermal runaway with LCO, LFP and NMC cathodes at 100% SOC. These parameters are important to be specified as under the same environmental conditions [9] and triggering method [38], the influence of cell type [39], cathode chemistry [40,41] and state of charge [42] on the vent gas components were shown to be significant. The 18650-type battery was chosen due to its wide applications and the well-documented literature on its physical behaviour during thermal runaway, including gas compositions [5,22,24]. The cathode materials were chosen due to their extensive applications in the battery industry [24,43] and the 100% SOC was considered in this study as this state poses a higher risk of thermal runaway and more severe subsequent hazards compared to other operational SOCs ( $0 \leq \text{SOC} \leq 100$ ) [12,15]. This work was carried out considering twelve fuels including  $\text{CH}_4$  (Methane),  $\text{C}_2\text{H}_6$  (Ethane),  $\text{C}_3\text{H}_8$  (Propane),  $\text{C}_4\text{H}_{10}$  (Butane),  $\text{C}_5\text{H}_{12}$  (Pentane),  $\text{C}_6\text{H}_6$  (Benzene),  $\text{C}_2\text{H}_4$  (Ethylene),  $\text{C}_3\text{H}_6$  (Propylene),  $\text{C}_2\text{H}_2$  (Acetylene),  $\text{CH}_3\text{OH}$  (Methanol),  $\text{C}_2\text{H}_5\text{OH}$  (Ethanol), and  $\text{H}_2$  (Hydrogen). These species were chosen based on their wide applications such as natural gas (blends of  $\text{CH}_4/\text{C}_2\text{H}_6/\text{C}_3\text{H}_8$ ) [44], liquefied petroleum gas ( $\text{C}_4\text{H}_{10}$ ) [45], fuel additives for combustion engines ( $\text{C}_5\text{H}_{12}$ ,  $\text{CH}_3\text{OH}$ ) [46,47], kerosene (blends of Decane/Propylbenzene/Propylcyclohexane) [48], low-emission turbine fuel ( $\text{C}_2\text{H}_4$ ) [49], hypersonic propulsion ( $\text{C}_2\text{H}_4$ ,  $\text{C}_3\text{H}_6$ ) [50], welding and metal cutting ( $\text{C}_2\text{H}_2$ ), biodiesel ( $\text{C}_2\text{H}_5\text{OH}$ ) [51] and low-emission engine fuel ( $\text{H}_2$ ) [52]. These applications resulted in a rich literature for their combustion kinetics solutions [18,53] that could be employed here. Although there are other fuels with higher number of carbons that could be considered in the current work, initial evaluations through 1-D premixed flame simulations did not indicate any superiority for them. Fig. 1 shows the variations of the mean absolute error (to be defined in Section 5) versus number of atoms in Alkanes, and it is seen that the error increased with increasing number of atoms. Therefore, high-carbon fuels ( $>6$ ) were not included in the analyses of this work.

The combustion properties of these fuels were compared to those of the original fuel mixtures through 1-D premixed and diffusion flames. Then, the obtained surrogate fuel were implemented in 3-D simulations to further validate the species mole fractions, gas temperature, radiative heat flux to the surroundings and CPU time.

The objective of this work is to replace the complex vent gases during thermal runaway of 18650-type lithium-ion batteries with a simplified fuel to streamline the modelling and reduce the computational demand while maintaining modelling accuracy. The findings of this research have the potential to contribute to the combustion modelling of battery fires and significantly accelerate computationally-expensive fully-coupled thermal runaway simulations [15] by reducing the number of combustion kinetics.

## 2. Governing equations

In this work, 1-D laminar premixed flame and 1-D counterflow diffusion flame were modelled to investigate the coupling between chemical kinetics and the thermodynamics of combustion [44]. Here, 1-D laminar premixed flame represents thermal runaway cases in which fuel and air, as oxidiser, are mixed initially and lead to explosions (e.g. Ref. [54]). Understanding laminar premixed flames is crucial as it forms a necessary foundation for studying turbulent flames [44]. In another scenario, the vent gases eject from the battery and meet with the air (e.g. Ref. [17]). The closest problem to this phenomenon is the 1-D counterflow diffusion flame.

For simulating the 1-D flames, the open-source Cantera chemical kinetics solver [55] was utilised. Cantera is a solver used for calculating thermodynamics, transport properties, and reaction rates in 0-D reactors and 1-D flames. To define a problem in Cantera, the user inputs the reaction kinetics, species thermodynamic data, and transport data. The problem is then defined using an input file and the flame properties such as species mole fractions, gas temperature and velocity are output.

Here, the flame was assumed to be stabilised in an asymmetric stagnation flow in a cylindrical coordinate, and the solution was computed along the stagnation streamline ( $r = 0$ ). By making these assumptions, the original 3-D governing equations were reduced to a simplified 1-D problem. Accordingly, the conservation laws of continuity, radial momentum, energy, and species can be derived as [55,56]

$$\frac{\partial(\rho u)}{\partial z} + 2\rho V = 0, \quad (1)$$

$$\rho u \frac{\partial V}{\partial z} + \rho V^2 = -\Lambda + \frac{\partial}{\partial z} \left( \mu \frac{\partial V}{\partial z} \right), \quad (2)$$

$$\rho c_p u \frac{\partial T}{\partial z} = \frac{\partial}{\partial z} \left( \lambda \frac{\partial T}{\partial z} \right) - \sum_k j_k c_{p,k} \frac{\partial T}{\partial z} - \sum_k h_k W_k \dot{\omega}_k, \quad (3)$$

$$\rho u \frac{\partial Y_k}{\partial z} = -\frac{\partial j_k}{\partial z} + W_k \dot{\omega}_k, \quad (4)$$

respectively. In Eq. (1),  $\rho$  is density,  $u$  is the axial velocity,  $V = v/r$  is the scaled radial velocity based on axial velocity,  $v$ , and radius,  $r$ . In Eq. (2),  $\Lambda$  is pressure eigenvalue and  $\mu$  is dynamic viscosity. In Eq. (3),  $c_p$  is heat capacity at constant pressure  $p$ ,  $T$  is temperature,  $\lambda$  is thermal conductivity,  $j_k$  is diffusive mass flux of species  $k$ ,  $c_{p,k}$  is specific heat capacity of species  $k$  and  $h_k$  is the enthalpy of species  $k$ . In Eq. (4),  $Y_k$  is mass fraction of species  $k$ ,  $W_k$  is the molecular weight of species  $k$  and  $\dot{\omega}_k$  is mole production rate of species  $k$ . The  $i$ th species diffusive mass flux,  $j_i$ , is computed according to the multicomponent formulation as [55]

$$j_i = \frac{\rho W_i}{W} \sum_{k=1}^N W_k D_{ik} \frac{\partial X_k}{\partial z} - \frac{D_i^T}{T} \frac{\partial T}{\partial z} \quad (5)$$

where  $D_{ki}$  is the multicomponent diffusion coefficient and  $D_i^T$  is the Soret diffusion coefficient. The effects of Soret diffusion on laminar flame speed were shown by Acampora et al. [57]. The mole fraction in Eq. (5) is calculated as

$$X_k = \frac{Y_k \bar{W}}{W_k}. \quad (6)$$

In the simulations, it was assumed that the tangential velocity was zero, and the fluid was treated as an ideal gas. At  $z = z_0$ , the gas

**Table 1**

Vent gas temperatures reported in the literature for cylindrical cells at 100% SOC and with LCO, LFP and NMC cathodes.

Reference	Battery type	Cathode	$T_g$ [K]	$T_{g,\text{avg}}$ [K]
Zhang et al. [58]	18 650	LCO	461.4	461.4
Fernandes et al. [6]	26 650	LFP	416.5	490.5
Yuan et al. [59]	18 650	LFP	548.2	
Ma et al. [60]	18 650	LFP	506.8	
Yan et al. [61]	18 650	NMC	433.2	494.7
Yuan et al. [59]	18 650	NMC	517.2	
Yuan et al. [59]	18 650	NMC	586.2	
Zhao et al. [54]	18 650	NMC	442.6	

was assumed to be in a stationary state for the premixed flame and in the diffusion flame, constant velocities were set for fuel and air boundaries. The temperature of fuel/air in premixed flame or that of fuel in diffusion flame at the boundaries was set at the battery vent gas temperature at the vent opening, before flaming, which is provided in **Table 1**. As presented in **Table 1**, multiple gas temperatures were reported in the literature for cylindrical cells with a single cathode material. Consequently, the simulations were conducted for the average temperatures ( $T_{g,\text{avg}}$ ) reported in the last column of **Table 1** to account for the temperature variability. The air temperature was set at 298.15 K in the diffusion flame. The pressure was 1 atm in both flames. The premixed flame was a freely propagating flame. For this case, zero gradient condition was assumed for both temperature and species mass fractions at the outlet boundary. The pressure eigenvalue and radial velocity were set to zero. At  $z = z_0$ , the temperature gradient, the scaled radial velocity,  $V$ , and the quantities  $\rho u$  and  $j_k$  were set to zero.

### 3. Kinetic modelling

The reaction rate of species  $k$  in Eqs. (3) and (4),  $\dot{\omega}_k$ , is calculated as [44]

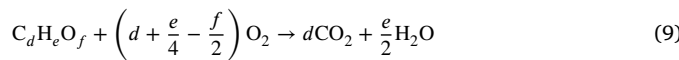
$$\dot{\omega}_k = \sum_{m=1}^M \kappa_m \prod_{n=1}^N c_n^{v_n} \quad (7)$$

where  $M$  is the number of reactions containing species  $k$ ,  $\kappa_m$  is the rate coefficient of reaction  $m$ ,  $N$  is the number of reactants in reaction  $m$ ,  $c_n$  is the molar concentration of reactant  $n$  and  $v_n$  is the stoichiometric coefficient of reactant  $n$ . The reaction rate,  $\kappa_m$ , is in an Arrhenius format. For the detailed kinetic mechanisms, the reaction rate is calculated from the elementary reactions as [44]

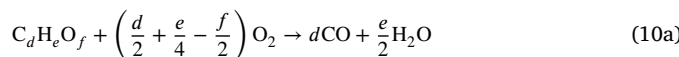
$$\kappa_m = A_m T^{\beta_m} \exp\left(\frac{-E_{a,m}}{RT}\right) \quad (8)$$

where for reaction  $m$ ,  $A_m$  is pre-exponential factor,  $T$  is temperature,  $\beta_m$  is the non-dimensional temperature exponent,  $E_{a,m}$  is activation energy and  $R = 8.314 \text{ J mol}^{-1} \text{ K}^{-1}$  is the ideal gas constant. In Eq. (8),  $A$ ,  $\beta$  and  $E_a$  are empirical coefficients [44].

Although detailed kinetics provide the most accurate solutions, identification of all the elementary reactions and their reaction rates is a difficult task and even if they are known precisely, implementing them in solving reacting flows is computationally expensive. The global reactions are often a convenient way of approximating the interactions of the detailed kinetic mechanisms. The one-step reaction is written as [18]



and the two-step reaction is written as



The rates of reactions shown in Eqs. (9), (10a) and (10b) can be expressed in an overall format as [18]

$$\dot{\omega}_{ov} = AT^\beta \exp\left(\frac{-E_a}{RT}\right) [\text{Fuel}]^a [\text{Oxidiser}]^b [\text{H}_2\text{O}]^c \quad (11)$$

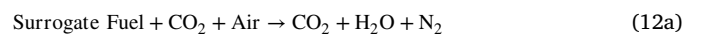
where the amounts in the brackets are the mole fractions of fuel or oxidiser, and  $a$ ,  $b$  and  $c$  are reaction orders of the corresponding components obtained from experimental measurements in flow reactors (not from the reaction stoichiometry). The cost of setting up and using detailed chemistry is high due to the numerous species and chemical stiffness. Consequently, the development of global chemistry and the identification of suitable surrogates become imperative.

### 4. Methodology

The vent gas compositions needed to be known first, but research in the literature showed that they were not consistent across different cases. Here, to organise the problem, the following assumptions were made: (1) the vent gases were in equilibrium, (2) the produced oxygen from cathode-involved reactions was consumed internally yielding CO and CO<sub>2</sub>, (3) electrolyte vapours observed in the early stages of thermal runaway [62] were discarded, (4) the vent gas compositions were at the steady state, representing the entire thermal runaway event and (5) the cell is pristine. These assumptions were previously confirmed by Cellier et al. [24] and were shown to be appropriate simplifying assumptions. Then, the compositions were collected from existing literature that studied the thermal runaway of 18650-type cells at 100% SOC with either LCO, LFP and NMC cathodes, which are presented in **Table 2**. As seen, a variety of compositions was detected in different works but the most common contains CH<sub>4</sub>, C<sub>2</sub>H<sub>4</sub>, C<sub>2</sub>H<sub>6</sub>, CO, CO<sub>2</sub> and H<sub>2</sub>. However, some other species such as C<sub>5</sub>H<sub>12</sub>, C<sub>6</sub>H<sub>6</sub>, C<sub>6</sub>H<sub>5</sub>CH<sub>3</sub> [63] and CH<sub>3</sub>OH [6] have been detected in the vent gases but for cell types other than 18650-type and with volumes less than 1%. Among all the reviewed works in **Table 2**, the studies of Golubkov et al. [5,33] provided the most common compositions. Golubkov et al. [5] reported the vent gas compositions for all three LCO, LFP, and NMC cathodes which match the cathodes considered in the current work. These compositions were also used in previous battery flame simulations and replicated experimental results [16] with good accuracy. Therefore, the compositions of Golubkov et al. [5] were employed here as the original fuel mixture which are presented in **Table 3**. This selection makes the analyses general and less complicated.

Here, the SanDiego detailed kinetic mechanism [23] was employed as the benchmark solution as this kinetic mechanism has demonstrated superior performance in combustion modelling of LIB flames [24]. For further evaluations, the reduced kinetic mechanisms developed by Cellier et al. [24] and the one- and two-step kinetics represented by Eqs. (9) and (10a), (10b), respectively, were considered for combustion modelling of the original mixture of **Table 3**.

Twelve fuels including CH<sub>4</sub>, C<sub>2</sub>H<sub>6</sub>, C<sub>3</sub>H<sub>8</sub>, C<sub>4</sub>H<sub>10</sub>, C<sub>5</sub>H<sub>12</sub>, C<sub>6</sub>H<sub>6</sub>, C<sub>2</sub>H<sub>4</sub>, C<sub>3</sub>H<sub>6</sub>, C<sub>2</sub>H<sub>2</sub>, CH<sub>3</sub>OH, C<sub>2</sub>H<sub>5</sub>OH and H<sub>2</sub> were employed as a surrogate fuel for the battery vent gas mixture (presented in **Table 3**). The preliminary analyses indicated that none of the surrogate fuels, solely, could produce CO<sub>2</sub> to the same extent as the original mixture. Therefore, the ejecting CO and CO<sub>2</sub> (presented in **Table 3**) were added to the surrogate fuel. The combustion of the surrogate fuel was considered in a one-step kinetic mechanism format as



where Air: O<sub>2</sub> + 3.76 N<sub>2</sub>. Here, all components listed in **Table 3**, except for CO and CO<sub>2</sub>, were replaced by the surrogate fuel. The corresponding volume fractions of CO<sub>2</sub> and CO reported in **Table 3** were assigned to the reactants' side of Eqs. (12a) and (12b), respectively. The remaining volume fractions were then allocated to the Surrogate Fuel in Eq. (12a).

**Table 2**

The thermal runaway vent gases reported in the literature for 18650-type cells at 100% SOC with either LCO, LFP or NMC cathodes.

Ref.	CH <sub>4</sub>	C <sub>2</sub> H <sub>2</sub>	C <sub>2</sub> H <sub>4</sub>	C <sub>2</sub> H <sub>6</sub>	C <sub>3</sub> H <sub>6</sub>	C <sub>3</sub> H <sub>8</sub>	C <sub>2</sub> H <sub>5</sub> F	C <sub>4</sub> <sup>a</sup>	CO	CO <sub>2</sub>	H <sub>2</sub>
Roth et al. [64]	✓	-	✓	✓	✓	✓	✓	✓	✓	✓	✓
Golubkov et al. [5]	✓	-	✓	✓	-	-	-	-	✓	✓	✓
Golubkov et al. [33]	✓	-	✓	✓	-	-	-	-	✓	✓	✓
FAA [35]	✓	-	✓	✓	✓	-	-	-	✓	✓	✓
Lammer et al. [41]	✓	✓	✓	✓	-	-	-	-	✓	✓	✓
Yuan et al. [59]	✓	✓	✓	✓	-	-	-	-	✓	✓	✓

<sup>a</sup> C<sub>4</sub> hydrocarbons

**Table 3**

The components of the vent gases from LIBs with LCO, NMC and LFP cathodes at 100% SOC reported by Golubkov et al. [5].

Cathode	Vent gas component [% mol]					
	C <sub>2</sub> H <sub>6</sub>	C <sub>2</sub> H <sub>4</sub>	CH <sub>4</sub>	CO	CO <sub>2</sub>	H <sub>2</sub>
LCO	1.2	7.7	8.6	27.6	24.9	30.0
LFP	0.3	6.8	4.1	4.8	53.0	30.9
NMC	0	8.2	6.8	13.0	41.2	30.8

For reactions (12a) and (12b), the one-step global kinetic mechanisms proposed by Westbrook et al. [18,53] for hydrocarbons and CO, and the mechanism proposed by Marinov et al. [52] for H<sub>2</sub>, were employed. The global rate expressions for the one-step reactions employed for original mixture and surrogate fuels are provided in Table 4. The global rate expressions for two-step reactions employed only for the original mixture are provided in Table 5, where H<sub>2</sub> had a one-step reaction, and  $\beta = 0$  was set according to [18,52,53]. The kinetic models presented in Tables 4 and 5 were derived in the reference works based on reaction dynamics and combustion kinetics. In this work, equivalence ratio and strain rate are defined as

$$\phi = \frac{[\text{Fuel}/\text{Air}]_{\text{actual}}}{[\text{Fuel}/\text{Air}]_{\text{stoichiometric}}} \quad (13)$$

and

$$\text{Strain Rate} = \frac{u_{\text{fuel}} + u_{\text{air}}}{\text{Domain Width}}, \quad (14)$$

respectively. In Eq. (13), the numerator is actual fuel to air mole fraction ratio and the stoichiometric ratio is in the denominator. With this definition, the combustion is fuel lean when  $0 < \phi < 1$  and is fuel rich when  $\phi > 1$  with  $\phi = 1$  at the stoichiometric condition. In Eq. (14),  $u_{\text{fuel}}$  and  $u_{\text{air}}$  are fuel and air stream velocity at the boundaries. It is notable that  $\phi$  is used for studying premixed flames as diffusion flames occur at  $\phi = 1$ , and strain rate is used for studying diffusion flames as the streams' properties are important in such flames. In this work, the domain width for premixed and diffusion flames were 40 mm and 80 mm, respectively [24].

In order to validate the current simulation setup, premixed and diffusion flames were simulated and compared with the literature. First, 1-D premixed flames of CH<sub>4</sub>/Air and LCO-mixture/Air, i.e., the combustion of LCO vent gas mixture presented in Table 3 with Air, were simulated using SanDiego mechanism and the laminar flame speeds were compared with the literature in Fig. 2. As seen, the results obtained from the simulations align well with the reference data with 6% to 7% differences, indicating a good agreement.

Then, a counterflow diffusion flame of vent gases with LCO cathode (represented in Table 3) was simulated and the results were compared to those of Cellier et al. [24]. Fig. 3 shows the comparisons of maximum temperature and integral heat release (IHR) with 0.8% and 7% errors, respectively.

The validations showed the correctness of the current simulations and allow for the expansion of the simulations to other fuels, which will be discussed in the following sections.

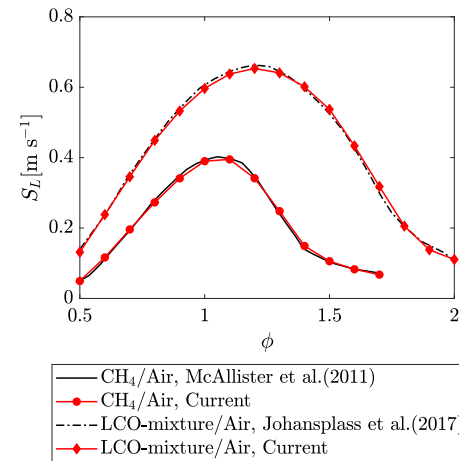


Fig. 2. Comparison of laminar flame speeds obtained from the current 1-D premixed flame simulations at  $T = 298.15$  K and  $p = 1$  atm, and those reported by McAllister et al. [65] and Johansplass et al. [21] with maximum 6% and 7% errors, respectively.

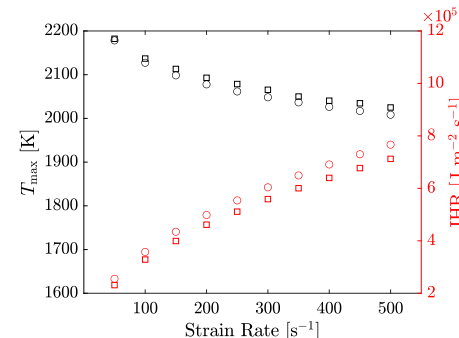


Fig. 3. Comparison of maximum temperature (black) and integral heat release (red) obtained from the current 1-D counterflow diffusion flame simulations (circle) and those reported by Cellier et al. [24] (square) with maximum 0.8% and 7% errors for  $T_{\max}$  and integral heat release, respectively. (For interpretation of the references to colour in this figure legend, the reader is referred to the web version of this article.)

## 5. Results and discussion

Twelve fuels including CH<sub>4</sub>, C<sub>2</sub>H<sub>6</sub>, C<sub>3</sub>H<sub>8</sub>, C<sub>4</sub>H<sub>10</sub>, C<sub>5</sub>H<sub>12</sub>, C<sub>6</sub>H<sub>6</sub>, C<sub>2</sub>H<sub>4</sub>, C<sub>3</sub>H<sub>6</sub>, C<sub>2</sub>H<sub>2</sub>, CH<sub>3</sub>OH, C<sub>2</sub>H<sub>5</sub>OH and H<sub>2</sub>, mixed with CO and CO<sub>2</sub>, were evaluated through 1-D premixed and 1-D counterflow diffusion flames as surrogate fuels for the battery vent gases (presented in Table 3). The kinetics of the surrogate fuels were based on Eqs. (12a) and (12b), and their performance was analysed versus the SanDiego detailed kinetic mechanism. Furthermore, the original mixture with one-step (Eq. (9)), two-step (Eqs. (10a), (10b)) and the reduced kinetic mechanisms [24] were included. Here, one-step (Eq. (9)) and two-step (Eqs. (10a) and (10b)) kinetic mechanisms of the original mixture

**Table 4**  
One-step kinetic rate expressions of gas combustion reactions.

Reaction	$A$ [cm <sup>3</sup> mol <sup>-1</sup> s <sup>-1</sup> ]	$E_a$ [kcal mol <sup>-1</sup> ]	$a$ [-]	$b$ [-]	$c$ [-]	Ref.
CH <sub>4</sub> + 2 O <sub>2</sub> → CO <sub>2</sub> + 2 H <sub>2</sub> O	1.3E9	48.4	-0.3	1.3	0	[18]
C <sub>2</sub> H <sub>6</sub> + 3.5 O <sub>2</sub> → 2 CO <sub>2</sub> + 3 H <sub>2</sub> O	1.1E12	30.0	0.1	1.65	0	[18]
C <sub>3</sub> H <sub>8</sub> + 5 O <sub>2</sub> → 3 CO <sub>2</sub> + 4 H <sub>2</sub> O	8.6E11	30.0	0.1	1.65	0	[18]
C <sub>4</sub> H <sub>10</sub> + 6.5 O <sub>2</sub> → 4 CO <sub>2</sub> + 5 H <sub>2</sub> O	7.4E11	30.0	0.15	1.6	0	[18]
C <sub>5</sub> H <sub>12</sub> + 8 O <sub>2</sub> → 5 CO <sub>2</sub> + 6 H <sub>2</sub> O	6.4E11	30.0	0.25	1.5	0	[18]
C <sub>6</sub> H <sub>6</sub> + 7.5 O <sub>2</sub> → 6 CO <sub>2</sub> + 3 H <sub>2</sub> O	2.0E11	30.0	-0.1	1.85	0	[18]
C <sub>2</sub> H <sub>4</sub> + 3 O <sub>2</sub> → 2 CO <sub>2</sub> + 2 H <sub>2</sub> O	2.0E12	30.0	0.1	1.65	0	[53]
C <sub>3</sub> H <sub>6</sub> + 4.5 O <sub>2</sub> → 3 CO <sub>2</sub> + 3 H <sub>2</sub> O	4.2E11	30.0	-0.1	1.85	0	[53]
C <sub>2</sub> H <sub>2</sub> + 2.5 O <sub>2</sub> → 2 CO <sub>2</sub> + H <sub>2</sub> O	6.5E12	30.0	0.5	1.25	0	[53]
CH <sub>3</sub> OH + 1.5 O <sub>2</sub> → CO <sub>2</sub> + 2 H <sub>2</sub> O	3.2E11	30.0	0.25	1.5	0	[18]
C <sub>2</sub> H <sub>5</sub> OH + 3 O <sub>2</sub> → 2 CO <sub>2</sub> + 3 H <sub>2</sub> O	1.5E12	30.0	0.25	1.5	0	[18]
H <sub>2</sub> + 0.5 O <sub>2</sub> → H <sub>2</sub> O	1.8E13	35.0	1.0	0.5	0	[52]
CO + 0.5 O <sub>2</sub> → CO <sub>2</sub>	3.98E14	40.0	1.0	0.25	0.5	[53]

**Table 5**  
Two-step kinetic rate expressions of gas combustion reactions of the original vent gas mixtures.

Reaction	$A$ [cm <sup>3</sup> mol <sup>-1</sup> s <sup>-1</sup> ]	$E_a$ [kcal mol <sup>-1</sup> ]	$a$ [-]	$b$ [-]	$c$ [-]	Ref.
CH <sub>4</sub> + 1.5 O <sub>2</sub> → CO + 2 H <sub>2</sub> O	2.8E9	48.4	-0.3	1.3	0	[18]
C <sub>2</sub> H <sub>6</sub> + 2.5 O <sub>2</sub> → 2 CO + 3 H <sub>2</sub> O	1.3E12	30.0	0.1	1.65	0	[18]
C <sub>2</sub> H <sub>4</sub> + 2 O <sub>2</sub> → 2 CO + 2 H <sub>2</sub> O	2.4E12	30.0	0.1	1.65	0	[53]
CO + 0.5 O <sub>2</sub> → CO <sub>2</sub>	3.98E14	40.0	1.0	0.25	0.5	[53]

(Table 3) are abbreviated as 1S Mix and 2S Mix, respectively, and the reference benchmark solution with SanDiego mechanism [23] and the reduced Cellier mechanism [24] are abbreviated as SanDiegoMech and CellierMech, respectively.

### 5.1. 1-D premixed laminar flame

With the premixed flame, the combustion characteristics of (constant-pressure) adiabatic flame temperature ( $T_{\text{adp}}$ ), H<sub>2</sub>O mole fraction ( $X_{\text{H}_2\text{O}}$ ), CO<sub>2</sub> mole fraction ( $X_{\text{CO}_2}$ ) and laminar flame speed ( $S_L$ ), obtained from one-step kinetic were compared with those from detailed kinetic mechanism. The selection of these parameters were due to their applications and the flame properties that can be resulted from. That is, the adiabatic flame temperature is a crucial parameter as it represents the maximum achievable temperature in a flame and characterises the heat emissions during combustion [65]. This parameter is essential in understanding the energy release and thermal behaviour of the fuel. The mole fractions of H<sub>2</sub>O and CO<sub>2</sub> products are important because they are the main combustion products and also they have a significant contribution to the flame's radiative properties due to their absorbance and emittance [66]. Therefore, studying their mole fractions helps in assessing the flame's radiative characteristics and then, flame propagation in battery fires. Finally, the laminar flame speed measures the fuel's explosive hazards [22]. It represents the speed at which the flame front propagates through the unburnt fuel-air mixture and provides insights into the potential hazards associated with the fuel.

In this work, the combustion of the vent gases was considered to occur in lean conditions after ejection, as previously shown to be the case in Ref. [32]. This is because the vent gases would dilute in the surrounding air, reaching the lower flammability limit. This assumption facilitates the temperature calculations as one-step kinetic mechanisms provide good accuracy in lean conditions but overestimate adiabatic flame temperature and laminar flame speed in the reach region. The reason is that in one-step kinetic mechanisms, the reaction products are only CO<sub>2</sub> and H<sub>2</sub>O. Therefore, the total heat of reaction is overpredicted in the rich condition. In contrast, in high-order kinetics, the existence of CO, H, O and OH in the products leads to a lower total heat of reaction in this condition [53].

Fig. 4 shows the adiabatic flame temperature, CO<sub>2</sub> and H<sub>2</sub>O mole fractions and laminar flame speed obtained from the 1-D premixed flame simulations. The fuel temperature was  $T_{\text{g,avg}}$ , presented in Table 1. In Fig. 4, it is evident that all the studied parameters exhibit an increase with equivalence ratio. This can be attributed to the fact

that as the equivalence ratio approaches unity (representing complete combustion), more CO<sub>2</sub> and H<sub>2</sub>O are produced, resulting in higher enthalpy of products and the release of more energy. This additional energy release leads to higher temperatures during the combustion process, consequently increasing the adiabatic flame temperature and gas expansion, which in turn leads to higher laminar flame speed.

Comparing different cases, Fig. 4 reveals that fuels with higher enthalpy of products exhibit higher adiabatic flame temperatures. The increase in temperature subsequently results in higher laminar flame speeds. It is seen that for instance, the surrogate mixture with H<sub>2</sub> produces more H<sub>2</sub>O and CO<sub>2</sub>. The observation can be attributed to the concept of Gibbs free energy change ( $\Delta G$ ). According to this principle, the negative  $\Delta G$  corresponds to a more favourable combustion reaction. For example, when comparing the oxidation of H<sub>2</sub> and CO in a mixture, the  $\Delta G$  of H<sub>2</sub> oxidation is lower than that of CO. As a result, H<sub>2</sub> requires less energy, allowing the remaining energy to be utilised for CO oxidation and the production of CO<sub>2</sub>. This concept can be extended to other similar cases.

### 5.2. 1-D counterflow diffusion flame

Simulating the diffusion flame, maximum temperature and integral heat release obtained from surrogate fuels with one-step kinetics were compared with those obtained from SanDiego mechanism. Here, the reason for studying integral heat release was that it accounts for the heat produced by the flame. The flame was simulated for strain rates, defined in Eq. (14), from 0.1 s<sup>-1</sup> to 500 s<sup>-1</sup>, to cover a wide range of flame conditions [24]. At every strain rate, the mass flow rates, and consequently, the densities of fuel and air streams were required in the simulations. The air density was 1.183 kg m<sup>-3</sup> (at 298.15 K) and the fuel densities at the corresponding  $T_{\text{g,avg}}$  are presented in Table 6.

Fig. 5 shows the maximum temperature and integral heat release obtained with the surrogate fuels and the original mixture with one- and two-step kinetics and also with the reduced kinetic mechanism. As seen, an important observation here is that flaming occurred over the whole range of strain rate with some fuels such as CH<sub>4</sub> and H<sub>2</sub> but, the flame extinguished at a certain strain rate for some other fuels such as C<sub>2</sub>H<sub>5</sub>OH. This happened because increasing the strain rate lead to an increase in the Damköhler number, subsequently decreasing the flame temperature. Therefore, the flame extinguished at a certain strain rate which varies for every fuel. The fuels that extinguished here could not be a candidate as the surrogate fuel, therefore, the analyses focused on those fuels that did not extinct. In Fig. 5, the discussion on the

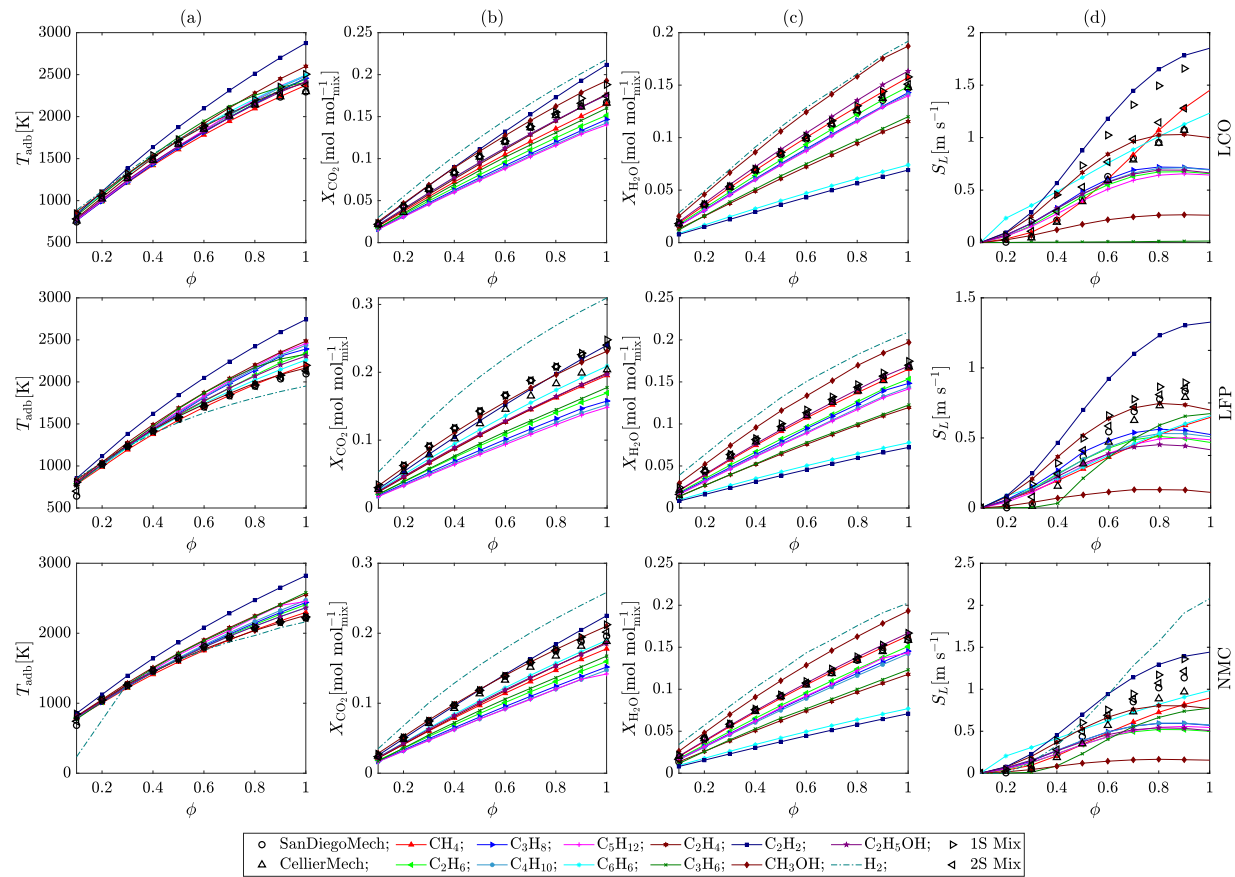


**Fig. 4.** Comparison of (a) adiabatic flame temperature, (b) CO<sub>2</sub> mole fraction, (c) H<sub>2</sub>O mole fraction and (d) laminar flame speed obtained from the 1-D premixed flame simulations with Surrogate Fuel/CO<sub>2</sub>/CO mixtures and different kinetic mechanisms for the original vent gas mixtures of LCO, LFP and NMC cells. SanDiegoMech is the reference solution.

**Table 6**

The densities of the original mixtures and Surrogate Fuel/CO<sub>2</sub>/CO mixtures for LCO, LFP and NMC cathodes cells at  $p = 1$  atm and at the corresponding average vent gas temperatures ( $T_{g,\text{avg}}$ ) reported in Table 1.

Original mixture	CO <sub>2</sub> /CO/ CH <sub>4</sub>	C <sub>2</sub> H <sub>2</sub>	C <sub>2</sub> H <sub>4</sub>	C <sub>2</sub> H <sub>6</sub>	C <sub>3</sub> H <sub>6</sub>	C <sub>3</sub> H <sub>8</sub>	C <sub>4</sub> H <sub>10</sub>	C <sub>5</sub> H <sub>12</sub>	C <sub>6</sub> H <sub>6</sub>	CH <sub>3</sub> OH	C <sub>2</sub> H <sub>5</sub> OH	H <sub>2</sub>	
LCO	0.61	0.69	0.82	0.84	0.87	1.02	1.04	1.22	1.40	1.47	0.89	1.07	0.52
LFP	0.69	0.78	0.88	0.90	0.92	1.05	1.07	1.22	1.37	1.43	0.94	1.09	0.63
NMC	0.63	0.55	0.83	0.85	0.87	1.01	1.03	1.19	1.35	1.41	0.90	1.05	0.56

values of the maximum temperature would be the same as the 1-D premixed flame, therefore, it is not repeated here. Another point of note is that, although one fuel has a higher maximum temperature profile compared to another fuel, its integral heat is lower. This phenomenon is observed, for example, with H<sub>2</sub> and C<sub>2</sub>H<sub>4</sub>. This occurred because the flame thickness may not be consistent between the two fuels and the flame with a greater thickness could have a higher integral heat release. Studying the flame thickness was beyond the scope of this work.

### 5.3. Performance analysis

To evaluate the performance of each case, the mean absolute error (MAE) was calculated as

$$\text{MAE}_\chi = \frac{1}{Z} \sum_{i=1}^Z \frac{|\chi_i - \chi_{\text{det},i}|}{\chi_{\text{det},i}} \quad (15)$$

where  $\chi$  is the parameter of interest (i.e.,  $T$ ,  $X_{\text{CO}_2}$ ,  $X_{\text{H}_2\text{O}}$  or  $S_L$ ),  $Z$  is number of points in the range of equivalence ratio/strain rate and the subscript “det” denotes to the detailed kinetic mechanism (the benchmark solution with SanDiego mechanism), respectively. The MAEs are reported in Figs. 6 to 8 for the 1-D premixed flame simulated with surrogate fuel and 1S Mix, 2S Mix and CellierMech [24]. It can

be observed from Fig. 6 that in the premixed flame, the CellierMech demonstrated the best performance for adiabatic flame temperature, H<sub>2</sub>O mole fraction and laminar flame speed, exhibiting errors ranging from 0.40% to 1.23%. However, this trend did not hold true for the LFP and NMC cases in Figs. 7 and 8, respectively, and 2S Mix had the best performance for the studied parameters. Another observation was the behaviour of C<sub>6</sub>H<sub>6</sub>. While the mean absolute errors for adiabatic flame temperature, CO<sub>2</sub> mole fraction, and laminar flame speed were low, they were considerably high for H<sub>2</sub>O mole fraction which could be due to the higher C/H ratio in the fuel and lower H<sub>2</sub>O production. This observation emphasises the importance of analysing  $T_{\text{adp}}$ ,  $X_{\text{H}_2\text{O}}$ ,  $X_{\text{CO}_2}$ , and  $S_L$  simultaneously to avoid drawing misleading conclusions.

To achieve an overall comparison, the average mean absolute error for every case is calculated as

$$\text{MAE}_{\text{avg}} = \frac{\text{MAE}_{T_{\text{adp}}} + \text{MAE}_{X_{\text{CO}_2}} + \text{MAE}_{X_{\text{H}_2\text{O}}} + \text{MAE}_{S_L}}{4} \quad (16)$$

where the subscripts  $T_{\text{adp}}$ ,  $X_{\text{CO}_2}$ ,  $X_{\text{H}_2\text{O}}$  and  $S_L$  refer to adiabatic flame temperate, CO<sub>2</sub> mole fraction, H<sub>2</sub>O mole fraction and laminar flame speed.

Fig. 9 shows the average errors calculated for every case. As seen in Fig. 9, the CH<sub>4</sub>/CO<sub>2</sub>/CO had the best performance for the LCO, LFP

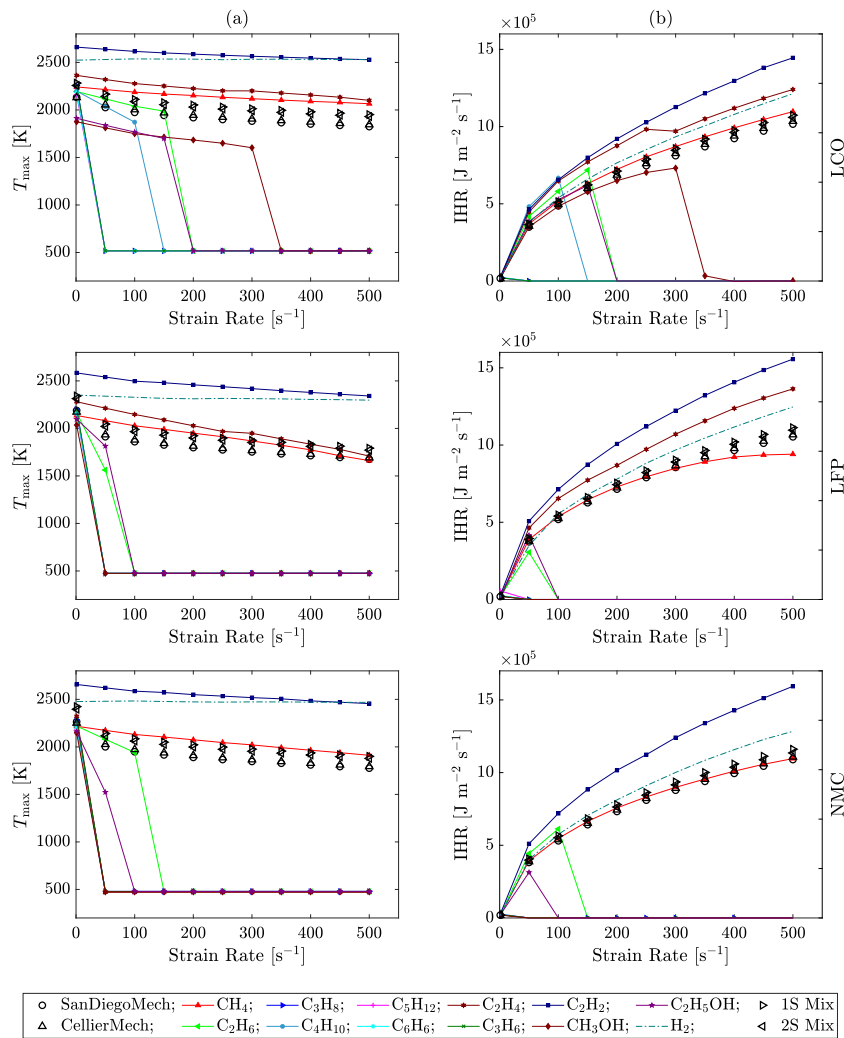


**Fig. 5.** Comparison of (a) maximum temperature and (b) integral heat release obtained from the 1-D counterflow diffusion flame simulations with Surrogate Fuel/CO<sub>2</sub>/CO mixtures and with different kinetic mechanisms for the original vent gas mixtures of LCO, LFP and NMC cells. SanDiegoMech is the reference solution.

and NMC cells, as the surrogate fuel. According to Fig. 9, although the reduced kinetic mechanism of Cellier et al. [24] had the best performance for LCO cathode cells against its counterparts, it is interesting to see that in contrast to the expectations, the two-step kinetic performs the best for LFP and NMC cathodes cells. This mechanism had 7.03% and 5.31% errors for LFP and NMC cathodes cells, respectively, while the corresponding errors obtained with the two-step kinetic were 2.57% and 2.55% for LFP and NMC cathodes cells, respectively. The reason for this observation could be rooted from the fact that the CellierMech was obtained for a different range of equivalence ratios,  $0.5 \leq \phi \leq 1.5$ , which led to be less accurate in the current range,  $0.1 \leq \phi \leq 1.0$ .

Fig. 10 shows the mean absolute errors of different fuels and kinetics for the maximum temperature and integral heat release in the counterflow diffusion flame. In Fig. 10, the fuels that extinguished over the range of strain rate are denoted with “Ext.”. Since they were no longer of interest, their errors were not included in the comparisons. The average MAEs are shown in Fig. 11. As seen, CH<sub>4</sub>/CO<sub>2</sub>/CO had the best performance as the surrogate fuel with average MAEs of 9.31%, 4.89% and 5.60% for the vent gases with LCO, LFP and NMC cathodes, respectively, and CellierMech had the best performance overall with the average MAEs smaller than 2%.

#### 5.4. 3-D validation

In this section, 3-D simulations of battery fires were conducted to assess the performance of the optimal surrogate fuel, CH<sub>4</sub>/CO<sub>2</sub>/CO. The

open-source solver Fire Dynamics Simulator (FDS) [67] was employed for the simulations. FDS is a CFD solver based on a low-Mach ( $\text{Ma} < 0.3$ ) format of Navier–Stokes equations for solving thermally-driven flows. In FDS, turbulence is treated using Large Eddy Simulation, and it can solve a wide variety of phenomena, including gas combustion, radiation, pyrolysis, and Lagrangian particle movement. The governing equations for the current FDS simulations are presented in the supplementary material, Appendix A. Here, the domain was a  $0.2 \times 0.2 \times 1$  m<sup>3</sup> cube, and the battery cell was assumed to be a vertical cylinder with a diameter of 0.018 m and a height of 0.065 m, placed in the bottom-centre of the domain. This geometry was previously utilised in Ref. [17]. After conducting a mesh independence study, the domain was meshed using cubic cells. The cell size was set to 1 mm around the battery and gradually increased with a ratio of 1:2 up to 4 mm in the far field, with the total number of 988543. The domain and the mesh independence study are presented in the supplementary material, Appendix A. The pressure at the boundaries on the sides and top of the domain was set to atmospheric pressure, known as “OPEN” in FDS terminology. The properties of cement were set for the floor and the properties of aluminium were set for the battery can from Ref. [68]. The vent gas was assumed to eject from the top of the battery.

The simulations were performed for cells with three different cathode materials of LCO, LFP, and NMC at 100% SOC. In FDS, users can directly input the heat release rate (HRR), and the solver converts it to fuel mass flow rate using predefined properties. For each cathode

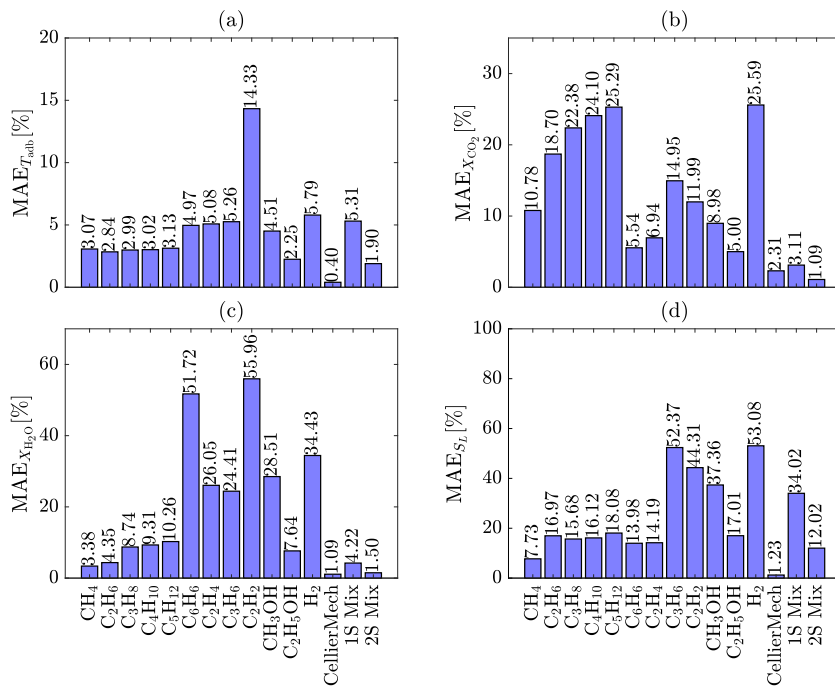


**Fig. 6.** Mean absolute errors of (a) adiabatic flame temperature, (b) CO<sub>2</sub> mole fraction, (c) H<sub>2</sub>O mole fraction and (d) laminar flame speed obtained from the 1-D premixed flame simulations with Surrogate Fuel/CO<sub>2</sub>/CO mixtures and with different kinetic mechanisms for the original vent gas mixture of LCO cell.

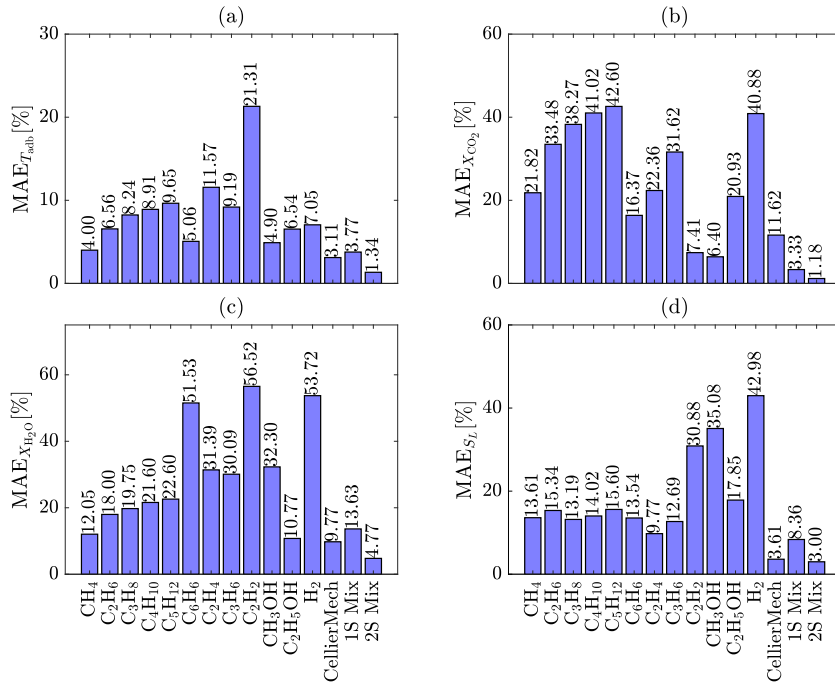


**Fig. 7.** Mean absolute errors of (a) adiabatic flame temperature, (b) CO<sub>2</sub> mole fraction, (c) H<sub>2</sub>O mole fraction and (d) laminar flame speed obtained from the 1-D premixed flame simulations with Surrogate Fuel/CO<sub>2</sub>/CO mixtures and with different kinetic mechanisms for the original vent gas mixture of LFP cell.

cell, several HRR curves have been experimentally measured in the literature [69–72] which are presented in the supplementary material, Appendix A. Due to their extensive variations from one experiment to another, and being variable versus time, it was decided here to employ the maximum value of the average curve for every cathode material. Accordingly, for LCO, LFP and NMC, the HRRs were set at 5.77, 2.82 and 5.03 kW, respectively. This approach helped to have identical cases in terms of heat release rate and it offers greater convenience

when comparing time-averaged data. Since the 3-D simulations were at constant HRRs, the (arbitrary) 60 s time was assumed to be large enough for averaging the associated turbulent phenomena.

Here, the results obtained with 1S Mix and the surrogate fuel were compared with those of 2S Mix, as the reference case, with the same kinetic parameters presented in Tables 4 and 5. The evaluations in this section involved comparing temperature, species mole fractions, radiative heat flux and CPU time. The reasons for analysing temperature and

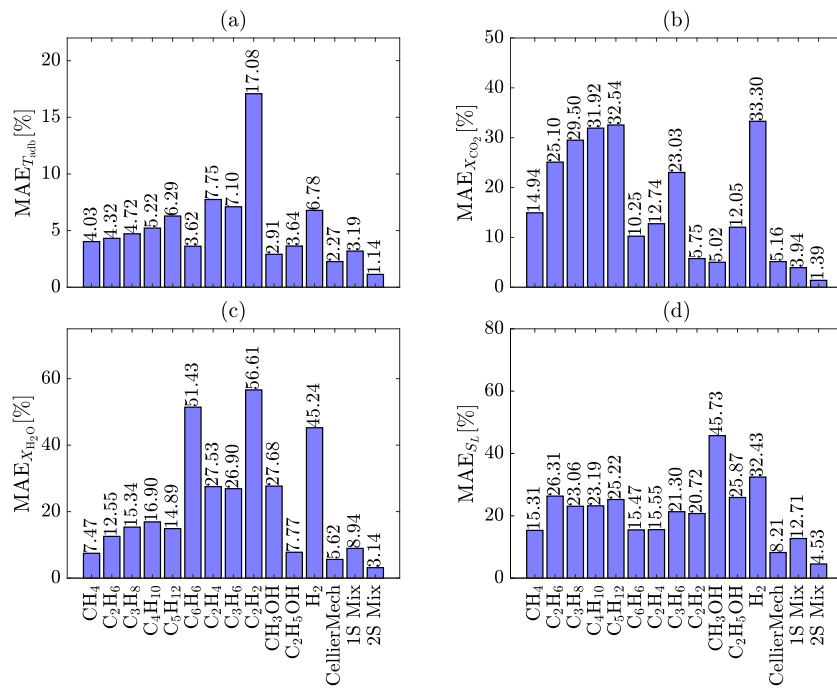


**Fig. 8.** Mean absolute errors of (a) adiabatic flame temperature, (b) CO<sub>2</sub> mole fraction, (c) H<sub>2</sub>O mole fraction and (d) laminar flame speed obtained from the 1-D premixed flame simulations with Surrogate Fuel/CO<sub>2</sub>/CO mixtures and with different kinetic mechanisms for the original vent gas mixture of NMC cell.

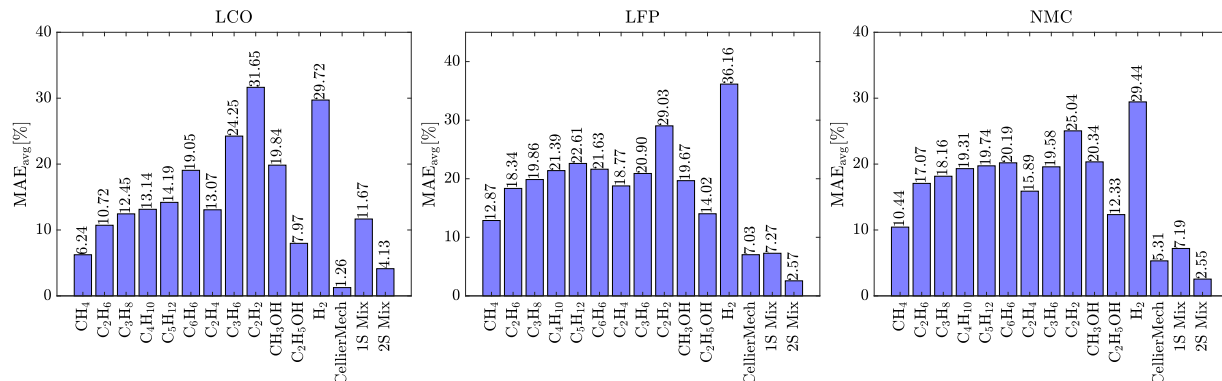


**Fig. 9.** The average mean absolute errors obtained from the 1-D premixed flame simulations with Surrogate Fuel/CO<sub>2</sub>/CO mixtures and with different kinetic mechanisms for the original vent gas mixtures of LCO, LFP and NMC cells.

mole fraction are consistent with those for 1-D flames. But, the inclusion of radiative heat flux in the comparisons is crucial because, similar to any fire scenarios, radiative heat transfer is primarily influenced by (the high) gas temperature, CO<sub>2</sub>, and H<sub>2</sub>O concentrations [66]. Additionally, radiative heat flux is important in the context of fire propagation since it is the dominant heat transfer mechanism in fires. Therefore, the heat fluxes were evaluated here to ensure that the surrogate fuel mixture can mimic those resulting from the original fuel mixture. Finally, the CPU times were analysed for every case. Here, the CPU time refers to the net total time in seconds spent on arithmetic and logic operations, excluding the time for input/output and data fetching/storing processes.

Figs. 12 to 14 show the time-averaged scalar fields of temperature, X<sub>CO<sub>2</sub></sub> and X<sub>H<sub>2</sub>O</sub> at x = 0 obtained from 3-D simulations for 60 s. As seen, the temperature and X<sub>H<sub>2</sub>O</sub> scalar fields had the maximum values at the flame front where the combustion happens and due to the ejection of CO<sub>2</sub>, X<sub>CO<sub>2</sub></sub> had high values within the flame region. The maximum temperatures of the current 3-D simulations obtained with 2S Max were 2058.6 K, 2140.1 K, and 1918.5 K with LCO, LFP, and NMC cathodes, respectively, which are comparable with the value

of 2000 °C [15,73] obtained by the same kinetic and 2300 K [24] obtained by the reduced kinetic mechanism. This comparison indicates that the current results fell within the range reported in the literature. Furthermore, Figs. 12 to 14 show that the compared scalar fields exhibit similarities between the results obtained from surrogate fuel, 1S Mix and 2S Mix; however, they are not identical. To quantify the differences and enable a more comprehensive comparison, a set of error functions with the 2S Mix as the benchmark solution was defined here.

To compare the cell values in different cases, a cell-by-cell error is defined as

$$\delta_c = \frac{1}{C} \sum_{j=1}^C \frac{|\chi_j - \chi_{2S,j}|}{\chi_{2S,j}} \times 100 \quad (17)$$

where  $\chi$  is the parameter of interest, C is total number of cells and subscript 2S denotes to the two-step kinetic (2S Mix). To compare the cases independent of the spatial distribution of the scalar fields, an overall error is defined as

$$\delta_o = \frac{|\sum_{j=1}^C \chi_j - \sum_{j=1}^C \chi_{2S,j}|}{\sum_{j=1}^C \chi_{2S,j}} \times 100. \quad (18)$$

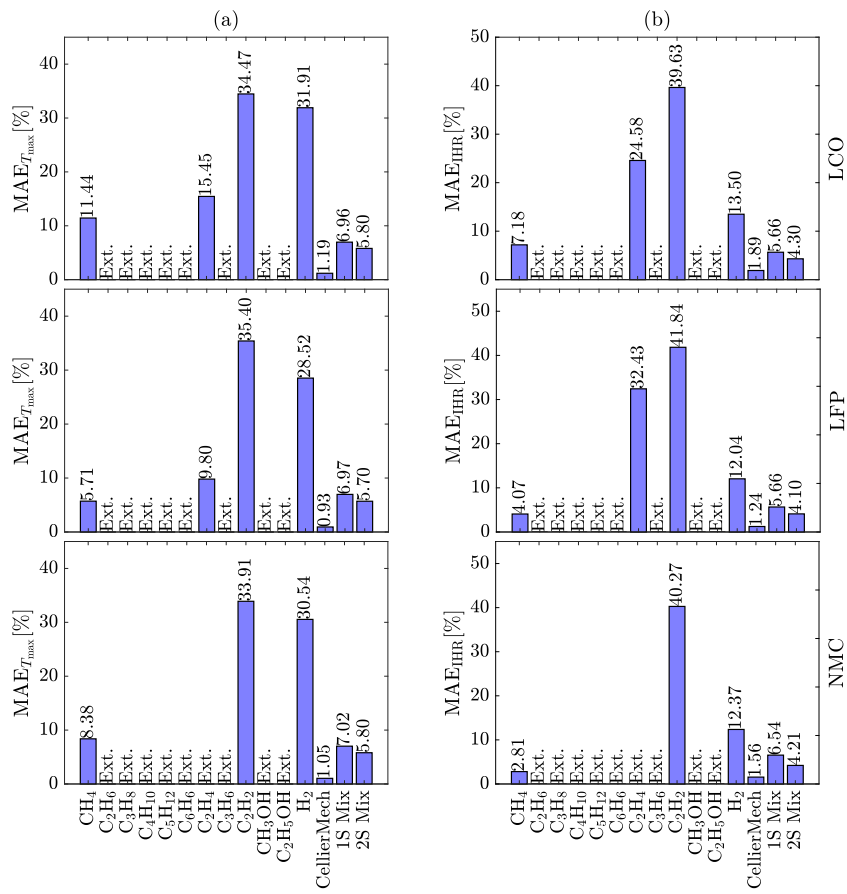


Fig. 10. Mean absolute errors of (a) maximum temperature and (b) integral heat release obtained from the 1-D counterflow diffusion flame simulations with Surrogate Fuel/CO<sub>2</sub>/CO mixtures and with different kinetic mechanisms for the original vent gas mixtures of LCO, LFP and NMC cells. The extinguished flames are labelled with “Ext.”.

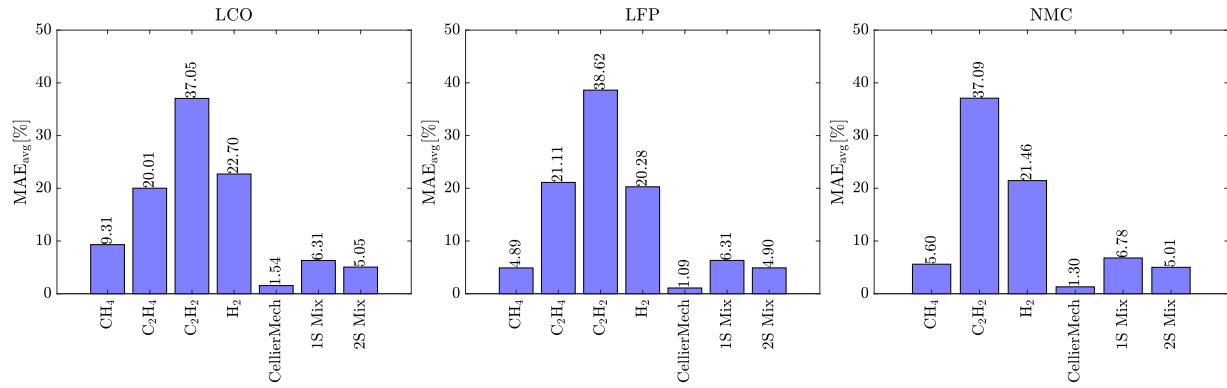


Fig. 11. The average mean absolute errors calculated for the studied kinetic mechanisms implemented in the 1-D counterflow diffusion flame simulations with Surrogate Fuel/CO<sub>2</sub>/CO mixtures and with different kinetic mechanisms for the original vent gas mixtures of LCO, LFP and NMC cells. The results are presented for the non-extincted flames.

The calculated errors are presented in Table 7. According to this table, the cell-by-cell errors resulting from surrogate fuel modelling exhibit a significant variation, indicating a dependence on the flame shape. The higher error suggests a greater deviation in flame shape compared to the reference solution, which can also be seen in Figs. 12 to 14. To assess the performance of the cases regardless of the flame shape, the overall error defined in Eq. (20) is a useful metric. The corresponding values presented in Table 7 indicates that the surrogate fuel was able to accurately predict the overall amounts of the reference solution. That is, the maximum error was found to be 12.2% for the CO<sub>2</sub> mole fraction with the LFP cathode, while the minimum error was 1.8% for the H<sub>2</sub>O mole fraction with the LCO cathode. Although there are no

similar simulations in the literature to directly compare the current errors, these values could be promising when compared to the battery fire simulations by Baird et al. [22] and Kong et al. [16], which reported maximum errors of 22% and 30% for combustion properties, respectively. To further analyse different chemistries, Table 7 presents the errors obtained from modelling with 1S Mix. In this case, the maximum cell-by-cell error was 21.3% for X<sub>CO<sub>2</sub></sub> with NMC cathode, while the maximum overall error was 6.5% for X<sub>CO<sub>2</sub></sub> with LCO cathode. The calculated errors, δ<sub>c</sub> and δ<sub>o</sub>, are provided in Table 7. The values confirmed the higher accuracy of 1S Mix, as expected, but they were very close to those obtained with the surrogate fuel.

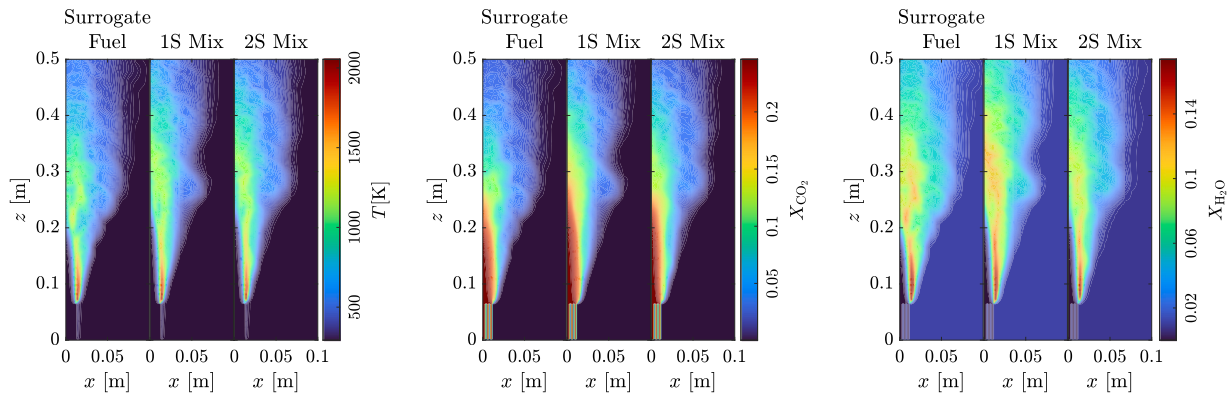


Fig. 12. Comparison of time-averaged temperature,  $\text{CO}_2$  and  $\text{H}_2\text{O}$  scalar fields obtained from 3-D simulations with different combustion chemistries with LCO cathode.

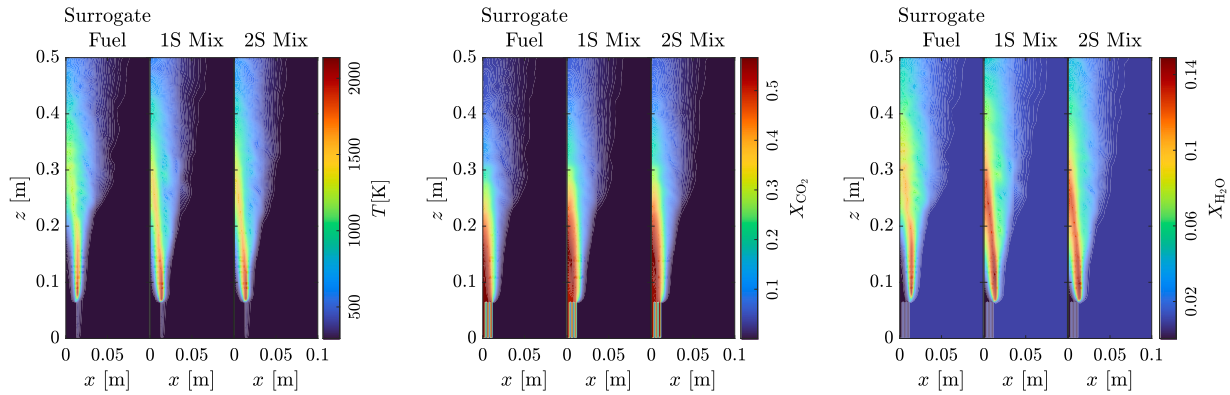


Fig. 13. Comparison of time-averaged temperature,  $\text{CO}_2$  and  $\text{H}_2\text{O}$  scalar fields obtained from 3-D simulations with different combustion chemistries with LFP cathode.

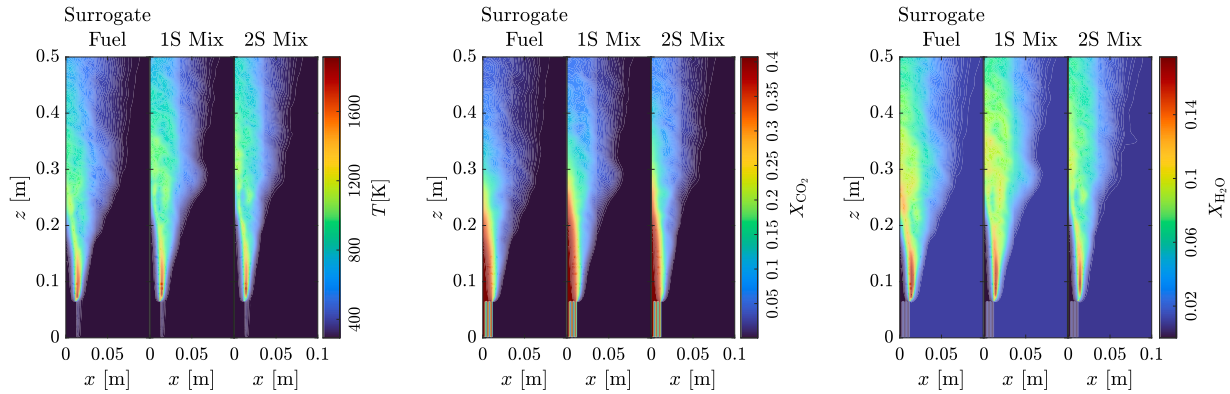


Fig. 14. Comparison of time-averaged temperature,  $\text{CO}_2$  and  $\text{H}_2\text{O}$  scalar fields obtained from 3-D simulations with different combustion chemistries with NMC cathode.

The consequence of inaccuracies in calculating temperature,  $X_{CO_2}$  and  $X_{H_2O}$  can be seen in the calculation of radiative heat flux, since these three parameters make the main contribution to modelling thermal radiation [74]. Fig. 15 compares the time-averaged radiative heat flux emitted from the flames modelled with different kinetics, reaching the surroundings of the battery up to 0.2 m.

To compare the values of radiative heat flux, an error is defined as

$$\delta_r = \frac{1}{B} \sum_{b=1}^B \frac{|\dot{q}_{r,b}'' - \dot{q}_{2S,r,b}''|}{\dot{q}_{2S,r,b}''} \times 100 \quad (19)$$

where  $B$  is the number of measuring points,  $\dot{q}_{r,b}''$  is the radiative heat flux obtained with 1S Mix or surrogate fuel and  $\dot{q}_{2S,r,b}''$  is the heat flux obtained with 2S Mix, as the reference solution. The values of  $\delta_r$  are reported in Table 7. The errors indicated that employing surrogate fuel

led to errors of 9%, 9.5% and 6.6% with LCO, LFP and NMC cathodes, respectively. However, the 1S Mix had 4.1%, 2.2% and 6.1% errors with LCO, LFP and NMC cathodes, respectively. Although error values indicated a favourable performance of 1S Mix, employing surrogate fuels could provide reasonably accurate results for radiative heat flux. Another observation here is that the radiative heat flux with LCO and NMC cells was higher than that of LFP cell, which could be due to the higher flame heat release rates.

According to the primary objective of this work, the utilisation of surrogate fuel was expected to lead to lower simulation times. In order to evaluate this influence, the CPU time difference is calculated as

$$\delta_{CPU} = \frac{t_{2S} - t}{t} \times 100 \quad (20)$$

where  $t$  and  $t_{2S}$  are the CPU times of the simulations with the chemistry in question and 2S Mix, respectively. The CPU times are reported in

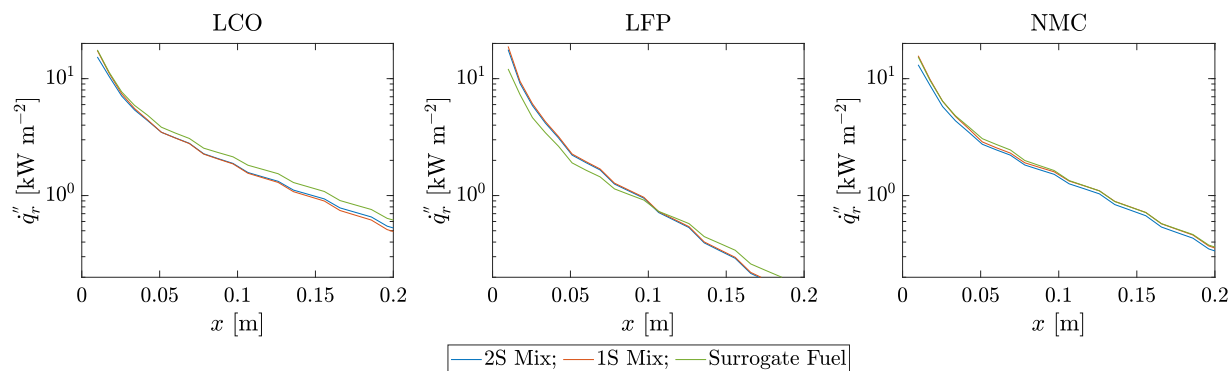


**Fig. 15.** Radiative heat flux reaching the surroundings obtained from the simulations with different combustion chemistries and cathodes. The y-axis is in logarithmic scale.

**Table 7**

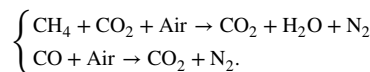
Errors and CPU time differences obtained from the surrogate fuel, CH<sub>4</sub>/CO<sub>2</sub>/CO, and 1S Mix solutions against the 2S Mix solution.

Chemistry	Cathode	$\delta_c$ [%]			$\delta_o$ [%]			$\delta_r$ [%]	$\delta_{CPU}$ [%]
		T	$X_{CO_2}$	$X_{H_2O}$	T	$X_{CO_2}$	$X_{H_2O}$		
Surrogate Fuel	LCO	14.3	26.2	10.2	2.7	7.6	1.8	9	55
	LFP	14.1	39.1	14	10.7	12.2	2.1	9.5	54
	NMC	17.3	36.4	11.7	3.0	9.7	3.1	6.6	46
1S Mix	LCO	8.7	12.1	6.3	2.1	6.5	1	4.1	27
	LFP	4.8	7	3.9	1.4	2.4	1.4	2.2	26
	NMC	10.1	21.3	7.4	2.3	4	0.4	6.1	37

**Table 7.** As reported, employing the surrogate fuels decreased the CPU times by 55%, 54%, and 46% with LCO, LFP, and NMC cathodes, respectively. These values indicate a substantial improvement in simulation speed achieved by using the surrogate fuel. However, the 1S Mix approach decreased the CPU times by 27%, 26% and 37% with LCO, LFP and NMC cathodes, respectively, which are still considerable amounts in heavy simulations.

## 6. Conclusion

This study aimed to replace the complex fuel mixture venting from a 18650-type lithium-ion battery in thermal runaway with a surrogate fuel to decrease computational costs while maintaining simulation accuracy. This research investigated twelve fuels, mixed with CO<sub>2</sub> and CO compositions from the original vent gas, by conducting 1-D premixed and 1-D counterflow diffusion flame simulations and some key parameters including temperature, CO<sub>2</sub> and H<sub>2</sub>O mole fractions, laminar flame speed, and total heat release, were analysed. Here, the premixed and diffusion flames represented explosion and flaming of the vent gases, respectively. The findings revealed that CH<sub>4</sub>/CO<sub>2</sub>/CO was the best surrogate fuel for the battery cells with LCO, LFP and NMC cathodes. Then, 3-D simulations were designed to examine the surrogate fuels, in terms of species mole fractions, temperature, radiative heat transfer and CPU time, in real applications. Implementing the surrogate mixture in 3-D simulations resulted in a maximum error of 12.2% in overall flame scalar fields, which corresponded to the mole fraction of CO<sub>2</sub> flame product with LFP cathode. The use of the surrogate fuel reduced CPU times by at least 46% compared to the two-step kinetic approach as the reference solution in 3-D cases. Furthermore, the radiative heat flux obtained from the surrogate fuel resulted in a maximum error of 9.5%. The combustion kinetics of the optimal surrogate fuel can be summarised as



This work can pave the way for exploring the use of surrogate fuels in various directions. Recommended future work would include

studying the vent gases of other battery forms, such as pouch and prismatic cells at 100% SOC. Additionally, 30% SOC is a favourable state of charge for storage and transportation due to its balance of safety and battery health [75], and the surrogate fuels could be studied for the vent gases at this SOC. Overall, the surrogate fuels could be extended to wider ranges of SOCs and battery forms, making them more applicable to a variety of scenarios. However, more experimental measurements are required in the future for such studies.

## CRediT authorship contribution statement

**Hosein Sadeghi:** Validation, Visualization, Investigation, Writing – original draft, Formal analysis, Methodology, Data curation, Conceptualization. **Francesco Restuccia:** Writing – review & editing, Conceptualization, Funding acquisition, Supervision, Project administration.

## Declaration of competing interest

The authors declare that they have no known competing financial interests or personal relationships that could have appeared to influence the work reported in this paper.

## Acknowledgements

This work was supported by King's College London NMES Ph.D. scholarship, UK and by the Faraday Institution, UK [grant number FIRG061]. The computational resources were provided by King's Computational Research, Engineering and Technology Environment (CREATE).

## Appendix A. Supplementary data

Supplementary material related to this article can be found online at <https://doi.org/10.1016/j.firesaf.2025.104464>.

## Data availability

Data will be made available on request.

## References

- [1] M. Fransson, L. Broche, M. Buckwell, J. Pfaff, H. Reid, C. Kirchner-Burles, M. Pham, S. Moser, A. Rack, S. Nau, S. Schopferer, D.P. Finegan, P. Shearing, Sidewall breach during lithium-ion battery thermal runaway triggered by cell-to-cell propagation visualized using high-speed X-ray imaging, *J. Energy Storage* 71 (2023) 108088, <http://dx.doi.org/10.1016/j.est.2023.108088>.
- [2] H. Niu, C. Chen, D. Ji, L. Li, Z. Li, Y. Liu, X. Huang, Thermal-runaway propagation over a linear cylindrical battery module, *Fire Technol.* 56 (2020) 2491–2507, <http://dx.doi.org/10.1007/s10694-020-00976-0>.
- [3] Y.-S. Duh, J.-H. Theng, C.-C. Chen, C.-S. Kao, Comparative study on thermal runaway of commercial 14500, 18650 and 26650 LiFePO<sub>4</sub> batteries used in electric vehicles, *J. Energy Storage* 31 (2020) 101580, <http://dx.doi.org/10.1016/j.est.2020.101580>.
- [4] H. Sadeghi, F. Restuccia, Kinetic modelling of thermal decomposition in lithium-ion battery components during thermal runaway, *J. Power Sources* 629 (2025) 236026, <http://dx.doi.org/10.1016/j.jpowsour.2024.236026>.
- [5] A.W. Golubkov, D. Fuchs, J. Wagner, H. Wiltsche, C. Stangl, G. Fauler, G. Voitic, A. Thaler, V. Hacker, Thermal-runaway experiments on consumer Li-ion batteries with metal-oxide and olivine-type cathodes, *RSC Adv.* 4 (2014) 3633–3642, <http://dx.doi.org/10.1039/C3RA45748F>.
- [6] Y. Fernandes, A. Bry, S. de Persis, Identification and quantification of gases emitted during abuse tests by overcharge of a commercial Li-ion battery, *J. Power Sources* 389 (2018) 106–119, <http://dx.doi.org/10.1016/j.jpowsour.2018.03.034>.
- [7] Q. Wang, B. Mao, S.I. Stolarov, J. Sun, A review of lithium ion battery failure mechanisms and fire prevention strategies, *Prog. Energ. Combust.* 73 (2019) 95–131, <http://dx.doi.org/10.1016/j.pecs.2019.03.002>.
- [8] M. Chen, J. Liu, Y. He, R. Yuan, J. Wang, Study of the fire hazards of lithium-ion batteries at different pressures, *Appl. Therm. Eng.* 125 (2017) 1061–1074, <http://dx.doi.org/10.1016/j.aplthermaleng.2017.06.131>.
- [9] A. García, J. Monsalve-Serrano, R.L. Sari, S. Martínez-Boggio, Influence of environmental conditions in the battery thermal runaway process of different chemistries: Thermodynamic and optical assessment, *Int. J. Heat. Mass. Transfer* 184 (2022) 122381, <http://dx.doi.org/10.1016/j.ijheatmasstransfer.2021.122381>.
- [10] Z. Wang, D. Ouyang, M. Chen, X. Wang, Z. Zhang, J. Wang, Fire behavior of lithium-ion battery with different states of charge induced by high incident heat fluxes, *J. Therm. Anal. Calorim.* 136 (2019) 2239–2247, <http://dx.doi.org/10.1007/s10973-018-7899-y>.
- [11] C.F. Lopez, J.A. Jeevarajan, P.P. Mukherjee, Experimental analysis of thermal runaway and propagation in lithium-ion battery modules, *J. Electrochem. Soc.* 162 (9) (2015) A1905, <http://dx.doi.org/10.1149/2.0921509jes>.
- [12] G. Zhong, H. Li, C. Wang, K. Xu, Q. Wang, Experimental analysis of thermal runaway propagation risk within 18650 lithium-ion battery modules, *J. Electrochem. Soc.* 165 (2018) A1925, <http://dx.doi.org/10.1149/2.0461809jes>.
- [13] T. Hatchard, D. MacNeil, A. Basu, J. Dahn, Thermal model of cylindrical and prismatic lithium-ion cells, *J. Electrochem. Soc.* 148 (2001) A755, <http://dx.doi.org/10.1149/1.1377592>.
- [14] X. Liu, Z. Wu, S.I. Stolarov, M. Denlinger, A. Masias, K. Snyder, A thermo-kinetic model of thermally-induced failure of a lithium ion battery: development, validation and application, *J. Electrochem. Soc.* 165 (2018) A2909, <http://dx.doi.org/10.1149/2.0111813jes>.
- [15] J. Kim, A. Mallarapu, D.P. Finegan, S. Santhanagopalan, Modeling cell venting and gas-phase reactions in 18650 lithium ion batteries during thermal runaway, *J. Power Sources* 489 (2021) 229496, <http://dx.doi.org/10.1016/j.jpowsour.2021.229496>.
- [16] D. Kong, G. Wang, P. Ping, J. Wen, A coupled conjugate heat transfer and CFD model for the thermal runaway evolution and jet fire of 18650 lithium-ion battery under thermal abuse, *ETransportation* 12 (2022) 100157, <http://dx.doi.org/10.1016/j.etrans.2022.100157>.
- [17] H. Sadeghi, F. Restuccia, Pyrolysis-based modelling of 18650-type lithium-ion battery fires in thermal runaway with LCO, LFP and NMC cathodes, *J. Power Sources* 603 (2024) 234480, <http://dx.doi.org/10.1016/j.jpowsour.2024.234480>.
- [18] C.K. Westbrook, F.L. Dryer, Chemical kinetic modeling of hydrocarbon combustion, *Prog. Energ. Combust.* 10 (1984) 1–57, [http://dx.doi.org/10.1016/0360-1285\(84\)90118-7](http://dx.doi.org/10.1016/0360-1285(84)90118-7).
- [19] J. Li, Z. Zhao, A. Kazakov, F.L. Dryer, An updated comprehensive kinetic model of hydrogen combustion, *Int. J. Chem. Kinet.* 36 (2004) 566–575, <http://dx.doi.org/10.1002/kin.20026>.
- [20] G.P. Smith, D.M. Golden, M. Frenklach, N.W. Moriarty, B. Eiteneer, M. Goldenberg, C.T. Bowman, R.K. Hanson, S. Song, J.W.C. Gardiner, V.V. Lissianski, Z. Qin, GRI-Mech 3.0, [http://www.me.berkeley.edu/gri\\_mech/](http://www.me.berkeley.edu/gri_mech/).
- [21] J. Johnsplass, M. Henriksen, K. Vaagsaether, J. Lundberg, D. Bjerketvedt, Simulation of burning velocities in gases vented from thermal run-a-way lithium ion batteries, in: Proc. 58th Conf. on Simulation and Modelling, 2017, pp. 157–161, <http://dx.doi.org/10.3384/ecp17138157>.
- [22] A.R. Baird, E.J. Archibald, K.C. Marr, O.A. Ezekoye, Explosion hazards from lithium-ion battery vent gas, *J. Power Sources* 446 (2020) 227257, <http://dx.doi.org/10.1016/j.jpowsour.2019.227257>.
- [23] F. Williams, Chemical-kinetic mechanisms for combustion applications, UC San Diego Mechanism web page, 2014, <http://web.engr.ucsd.edu/mae/groups/combustion/index.html>.
- [24] A. Cellier, F. Duchaine, T. Poinsot, G. Okyay, M. Leyko, M. Pallud, An analytically reduced chemistry scheme for large eddy simulation of lithium-ion battery fires, *Combust. Flame* 250 (2023) 112648, <http://dx.doi.org/10.1016/j.combustflame.2023.112648>.
- [25] Y. Wu, S. Panigrahy, A.B. Sahu, C. Bariki, J. Beeckmann, J. Liang, A.A. Mohamed, S. Dong, C. Tang, H. Pitsch, Z. Huang, H.J. Curran, Understanding the antagonistic effect of methanol as a component in surrogate fuel models: A case study of methanol/n-heptane mixtures, *Combust. Flame* 226 (2021) 229–242, <http://dx.doi.org/10.1016/j.combustflame.2020.12.006>.
- [26] O. Mathieu, C.M. Grégoire, M.A. Turner, D.J. Mohr, S.A. Alturaifi, J.C. Thomas, E.L. Petersen, Experimental investigation of the combustion properties of an average thermal runaway gas mixture from Li-ion batteries, *Energ. Fuel.* 36 (2022) 3247–3258, <http://dx.doi.org/10.1021/acs.energyfuels.1c04057>.
- [27] W. Sun, B. Yang, N. Hansen, C.K. Westbrook, F. Zhang, G. Wang, K. Moshammer, C.K. Law, An experimental and kinetic modeling study on dimethyl carbonate (DMC) pyrolysis and combustion, *Combust. Flame* 164 (2016) 224–238, <http://dx.doi.org/10.1016/j.combustflame.2015.11.019>.
- [28] W.K. Metcalfe, S.M. Burke, S.S. Ahmed, H.J. Curran, A hierarchical and comparative kinetic modeling study of C<sub>1</sub>-C<sub>5</sub> hydrocarbon and oxygenated fuels, *Int. J. Chem. Kinet.* 45 (2013) 638–675, <http://dx.doi.org/10.1002/kin.20802>.
- [29] E. Ranzi, C. Cavallotti, A. Cuoci, A. Frassoldati, M. Pelucchi, T. Faravelli, New reaction classes in the kinetic modeling of low temperature oxidation of n-alkanes, *Combust. Flame* 162 (2015) 1679–1691, <http://dx.doi.org/10.1016/j.combustflame.2014.11.030>.
- [30] H. Wang, E. Dames, B. Sirjean, D. Sheen, R. Tangko, A. Violi, J. Lai, F. Egolfopoulos, D. Davidson, R. Hanson, et al., A high-temperature chemical kinetic model of n-alkane (up to n-dodecane), cyclohexane, and methyl-, ethyl-, n-propyl and n-butyl-cyclohexane oxidation at high temperatures, 2010, JetSurF Version 2.0, <http://web.stanford.edu/group/haiwanglab/JetSurF/JetSurF2.0/index.html>.
- [31] D. Healy, D. Kalitan, C. Aul, E. Petersen, G. Bourque, H. Curran, Oxidation of C<sub>1</sub>-C<sub>5</sub> alkane quaternary natural gas mixtures at high pressures, *Energ. Fuel.* 24 (2010) 1521–1528, <http://dx.doi.org/10.1021/ef9011005>.
- [32] R. Yu, J. Liu, W. Liang, C.K. Law, H. Wang, M. Ouyang, On flammability limits of battery vent gas: Role of diffusion, radiation and chemical kinetics, *Combust. Flame* 249 (2023) 112631, <http://dx.doi.org/10.1016/j.combustflame.2023.112631>.
- [33] A.W. Golubkov, S. Scheikl, R. Planteu, G. Voitic, H. Wiltsche, C. Stangl, G. Fauler, A. Thaler, V. Hacker, Thermal runaway of commercial 18650 Li-ion batteries with LFP and NCA cathodes-impact of state of charge and overcharge, *RSC Adv.* 5 (70) (2015) 57171–57186, <http://dx.doi.org/10.1039/C5RA05897J>.
- [34] S. Koch, A. Fill, K.P. Birke, Comprehensive gas analysis on large scale automotive lithium-ion cells in thermal runaway, *J. Power Sources* 398 (2018) 106–112, <http://dx.doi.org/10.1016/j.jpowsour.2018.07.051>.
- [35] T. Maloney, Lithium Battery Thermal Runaway Vent Gas Analysis, Tech. Rep. DOT/FAA/TC-15/59, U.S. Department of Transportation, 2016, <https://www.fire.tc.faa.gov/pdf/TC-15-59.pdf>.
- [36] C.M. Vendra, A.V. Shelke, J.E. Buston, J. Gill, D. Howard, E. Read, A. Abaza, B. Cooper, J.X. Wen, Numerical and experimental characterisation of high energy density 21700 lithium-ion battery fires, *Process. Saf. Env.* 160 (2022) 153–165, <http://dx.doi.org/10.1016/j.psep.2022.02.014>.
- [37] S. Voigt, F. Sträubig, A. Kwade, J. Zehfuß, C. Knaust, An empirical model for lithium-ion battery fires for CFD applications, *Fire Saf. J.* 135 (2023) 103725, <http://dx.doi.org/10.1016/jfiresaf.2022.103725>.
- [38] O. Willstrand, M. Pushp, P. Andersson, D. Brandell, Impact of different Li-ion cell test conditions on thermal runaway characteristics and gas release measurements, *J. Energy Storage* 68 (2023) 107785, <http://dx.doi.org/10.1016/j.est.2023.107785>.
- [39] C. Essl, A. Golubkov, A. Fuchs, Comparing different thermal runaway triggers for two automotive lithium-ion battery cell types, *J. Electrochem. Soc.* 167 (13) (2020) 130542, <http://dx.doi.org/10.1149/1945-7111/abbe5a>.
- [40] Q. Wang, P. Ping, X. Zhao, G. Chu, J. Sun, C. Chen, Thermal runaway caused fire and explosion of lithium ion battery, *J. Power Sources* 208 (2012) 210–224, <http://dx.doi.org/10.1016/j.jpowsour.2012.02.038>.
- [41] M. Lammer, A. Königseder, V. Hacker, Holistic methodology for characterisation of the thermally induced failure of commercially available 18650 lithium ion cells, *RSC Adv.* 7 (39) (2017) 24425–24429, <http://dx.doi.org/10.1039/C7RA02635H>.
- [42] Q. Zhang, J. Niu, Z. Zhao, Q. Wang, Research on the effect of thermal runaway gas components and explosion limits of lithium-ion batteries under different charge states, *J. Energy Storage* 45 (2022) 103759, <http://dx.doi.org/10.1016/j.est.2021.103759>.
- [43] Y.-S. Duh, Y. Sun, X. Lin, J. Zheng, M. Wang, Y. Wang, X. Lin, X. Jiang, Z. Zheng, S. Zheng, G. Yu, Characterization on thermal runaway of commercial 18650 lithium-ion batteries used in electric vehicles: A review, *J. Energy Storage* 41 (2021) 102888, <http://dx.doi.org/10.1016/j.est.2021.102888>.

- [44] S. Turns, D.C. Haworth, An Introduction to Combustion: Concepts and Applications, McGraw-Hill Companies New York, NY, USA, 2021, <https://www.mheducation.com/highered/product/introduction-combustion-concepts-applications-turns-haworth/M9781260477696.html>.
- [45] V. Savelieva, A.M. Savel'ev, N.S. Titova, Kinetic mechanism of ignition of propane-butane mixtures at low and high temperatures: Development and application, *Combust. Shock+* 59 (1) (2023) 1–21, <http://dx.doi.org/10.1134/S001050822301001X>.
- [46] M. Elkelawy, H. Alm-Eldin Bastawissi, E. El Shenawy, M. Taha, H. Panchal, K.K. Sadasivuni, Study of performance, combustion, and emissions parameters of DI-diesel engine fueled with algae biodiesel/diesel/n-pentane blends, *Energ. Convers. Manag.* 10 (2021) 100058, <http://dx.doi.org/10.1016/j.ecmx.2020.100058>.
- [47] J. Li, Z. Zhao, A. Kazakov, M. Chaos, F.L. Dryer, J.J. Scire Jr., A comprehensive kinetic mechanism for CO, CH<sub>2</sub>O, and CH<sub>3</sub>OH combustion, *Int. J. Chem. Kinet.* 39 (3) (2007) 109–136, <http://dx.doi.org/10.1002/kin.20218>.
- [48] P. Dagaut, On the kinetics of hydrocarbons oxidation from natural gas to kerosene and diesel fuel, *Phys. Chem. Chem. Phys.* 4 (11) (2002) 2079–2094, <http://dx.doi.org/10.1039/B110787A>.
- [49] S.-Y. Lee, S.R. Turns, R.J. Santoro, Measurements of soot, OH, and PAH concentrations in turbulent ethylene/air jet flames, *Combust. Flame* 156 (12) (2009) 2264–2275, <http://dx.doi.org/10.1016/j.combustflame.2009.09.005>.
- [50] B. Sarnacki, G. Esposito, R. Krauss, H. Chelliah, Extinction limits and associated uncertainties of nonpremixed counterflow flames of methane, ethylene, propylene and n-butane in air, *Combust. Flame* 159 (3) (2012) 1026–1043, <http://dx.doi.org/10.1016/j.combustflame.2011.09.007>.
- [51] J. Hill, E. Nelson, D. Tilman, S. Polasky, D. Tiffany, Environmental, economic, and energetic costs and benefits of biodiesel and ethanol biofuels, *Proc. Natl. Acad. Sci. USA* 103 (30) (2006) 11206–11210, <http://dx.doi.org/10.1073/pnas.0604600103>.
- [52] N.M. Marinov, C.K. Westbrook, W.J. Pitz, Detailed and global chemical kinetics model for hydrogen, in: 8th International Symposium on Transport Properties, San Francisco, CA, USA, 1995, <https://www.osti.gov/biblio/90098>.
- [53] C.K. Westbrook, F.L. Dryer, Simplified reaction mechanisms for the oxidation of hydrocarbon fuels in flames, *Combust. Sci. Technol.* 27 (1981) 31–43, <http://dx.doi.org/10.1080/00102208108946970>.
- [54] C. Zhao, J. Sun, Q. Wang, Thermal runaway hazards investigation on 18650 lithium-ion battery using extended volume accelerating rate calorimeter, *J. Energy Storage* 28 (2020) 101232, <http://dx.doi.org/10.1016/j.est.2020.101232>.
- [55] D.G. Goodwin, H.K. Moffat, I. Schoegl, R.L. Speth, B.W. Weber, Cantera: An object-oriented software toolkit for chemical kinetics, thermodynamics, and transport processes, 2022, Version 2. 6. 0. <https://www.cantera.org>.
- [56] R.J. Kee, M.E. Coltrin, P. Glarborg, Chemically reacting flow: Theory and practice, in: Chemically Reacting Flow: Theory and Practice, John Wiley & Sons, Hoboken, NJ, 2003, <https://onlinelibrary.wiley.com/doi/book/10.1002/0471461296>.
- [57] L. Acampora, F.S. Marra, Effects of soot diffusion on the exergy losses in hydrogen laminar premixed flames, *Int. J. Hydrot. Energ.* 48 (2023) 28539–28548, <http://dx.doi.org/10.1016/j.ijhydene.2023.03.404>.
- [58] Q. Zhang, T. Liu, C. Hao, Y. Qu, J. Niu, Q. Wang, D. Chen, In situ Raman investigation on gas components and explosion risk of thermal runaway emission from lithium-ion battery, *J. Energy Storage* 56 (2022) 105905, <http://dx.doi.org/10.1016/j.est.2022.105905>.
- [59] L. Yuan, T. Dubaniewicz, I. Zlochower, R. Thomas, N. Rayyan, Experimental study on thermal runaway and vented gases of lithium-ion cells, *Process. Saf. Env.* 144 (2020) 186–192, <http://dx.doi.org/10.1016/j.psep.2020.07.028>.
- [60] Y. Ma, Y. Zhang, N. Chen, Z. Lai, L. Zhu, S. Chen, Z. Teng, N. Zhang, B. Mao, Thermal runaway propagation behavior and cooling effect of water mist within a 18650-type LiFePO<sub>4</sub> battery module under different conditions, *Process. Saf. Env.* 185 (2024) 1362–1372, <http://dx.doi.org/10.1016/j.psep.2024.04.002>.
- [61] H. Yan, K.C. Marr, O.A. Ezekoye, Towards fire forensic characteristics of failed cylindrical format lithium-Ion cells and batteries, *Fires Technol.* 57 (2021) 1723–1752, <http://dx.doi.org/10.1007/s10694-020-01079-6>.
- [62] Q. Zhang, T. Liu, Q. Wang, Experimental study on the influence of different heating methods on thermal runaway of lithium-ion battery, *J. Energy Storage* 42 (2021) 103063, <http://dx.doi.org/10.1016/j.est.2021.103063>.
- [63] V. Somandepalli, K. Marr, Q. Horn, Quantification of combustion hazards of thermal runaway failures in lithium-ion batteries, *SAE Int. J. Altern. Powertrains* 3 (2014) 98–104, <http://dx.doi.org/10.4271/2014-01-1857>.
- [64] E.P. Roth, Abuse response of 18650 Li-ion cells with different cathodes using EC: EMC/LiPF<sub>6</sub> and EC: PC: DMC/LiPF<sub>6</sub> electrolytes, *ECS Trans.* 11 (19) (2008) 19, <http://dx.doi.org/10.1149/1.2897969>.
- [65] S. McAllister, J.-Y. Chen, A.C. Fernandez-Pello, Fundamentals of combustion processes, in: Fundamentals of Combustion Processes, Springer New York, New York, NY, 2011, [http://dx.doi.org/10.1007/978-1-4419-7943-8\\_6](http://dx.doi.org/10.1007/978-1-4419-7943-8_6).
- [66] H. Sadeghi, S. Hostikka, G.C. Fraga, H. Bordbar, Weighted-sum-of-gray-gases models for non-gray thermal radiation of hydrocarbon fuel vapors, CH<sub>4</sub>, CO and soot, *Fire Saf. J.* 125 (2021) 103420, <http://dx.doi.org/10.1016/j.firesaf.2021.103420>.
- [67] K. McGrattan, S. Hostikka, R. McDermott, J. Floyd, C. Weinschenk, K. Overholt, Fire dynamics simulator user's guide, NIST Spec. Publ. 1019 (2013) 1–339, [https://github.com/firemodels/fds/releases/download/FDS-6.8.0/FDS\\_User\\_Guide.pdf](https://github.com/firemodels/fds/releases/download/FDS-6.8.0/FDS_User_Guide.pdf).
- [68] M.J. Hurley, D.T. Gottuk, J.R. Hall Jr., K. Harada, E.D. Kuligowski, M. Puchovsky, J.M. Watts Jr., C.J. Wieczorek, et al., SFPE Handbook of Fire Protection Engineering, Springer, 2015, <http://dx.doi.org/10.1007/978-1-4939-2565-0>.
- [69] M. Chen, D. Zhou, X. Chen, W. Zhang, J. Liu, R. Yuen, J. Wang, Investigation on the thermal hazards of 18650 lithium ion batteries by fire calorimeter, *J. Therm. Anal. Calorim.* 122 (2) (2015) 755–763, <http://dx.doi.org/10.1007/s10973-015-4751-5>.
- [70] Y. Fu, S. Lu, K. Li, C. Liu, X. Cheng, H. Zhang, An experimental study on burning behaviors of 18650 lithium ion batteries using a cone calorimeter, *J. Power Sources* 273 (2015) 216–222, <http://dx.doi.org/10.1016/j.jpowsour.2014.09.039>.
- [71] A.O. Said, Dynamics and Hazards of Cascading Failure in Lithium Ion Cell Arrays: Analysis, Passive Mitigation, and Active Suppression (Ph.D. thesis), University of Maryland, College Park, 2020, p. 299, <https://www.proquest.com/dissertations-theses/dynamics-hazards-cascading-failure-lithium-ion/docview/2430414784/se-2>.
- [72] W. Wang, T. He, S. He, T. You, F. Khan, Modeling of thermal runaway propagation of NMC battery packs after fast charging operation, *Process. Saf. Env.* 154 (2021) 104–117, <http://dx.doi.org/10.1016/j.psep.2021.08.006>.
- [73] Y. Takagishi, Y. Tozuka, T. Yamamoto, T. Yamaue, Heating simulation of a Li-ion battery cylindrical cell and module with consideration of gas ejection, *Energy Rep.* 8 (2022) 3176–3188, <http://dx.doi.org/10.1016/j.egyr.2022.02.086>.
- [74] H. Sadeghi, Numerical Modeling of Spectral Radiative Properties of Fuel Vapors in Fires (LicSc thesis), Aalto University, 2022, <https://urn.fi/URN:NBN:fi:aalto-202205053018>.
- [75] Q. Zhang, J. Niu, J. Yang, T. Liu, F. Bao, Q. Wang, In-situ explosion limit analysis and hazards research of vent gas from lithium-ion battery thermal runaway, *J. Energy Storage* 56 (2022) 106146, <http://dx.doi.org/10.1016/j.est.2022.106146>.